Hydro-Geophysical Assessment of Sub Surface to Improve Groundwater Models (Sardon Case Study, Spain)

Abubeker Ali Mohammed

March, 2010

Hydro-Geophysical Assessment of Sub Surface to Improve Groundwater Models
(Sardon Case Study, Spain)

By

Abubeker Ali Mohammed

Thesis submitted to the International Institute for Geo-information Science and Earth Observation in partial fulfilment of the requirements for the degree of Master of Science in Geo-information Science and Earth Observation, Water Resource and Environmental Management, Specialisation: Groundwater Resource Assessment and Management

Thesis Assessment Board

Prof. Dr. Bob Su, ITC (Chairman)
Prof. Dr. Okke Batelaan, Vrije Universiteit Brussel (External Examinar)
Dr. Ir. Maciek W. Lubczynski, ITC (1st Supervisor)
Dr. Mark van der Meijde, ITC (2nd Supervisor)
MSc. Alain Pascal Francés (Advisor)

INTERNATIONAL INSTITUTE FOR GEO-INFORMATION SCIENCE AND EARTH OBSERVATION
ENSCHEDE, THE NETHERLANDS

Disclaimer

This document describes work undertaken as part of a programme of study at the International Institute for Geo-information Science and Earth Observation. All views and opinions expressed therein remain the sole responsibility of the author, and do not necessarily represent those of the institute.

Abstract

The Sardon catchment is characterized by granitic hard rocks. Hard rock aquifers particularly in granitic terrain have extremely different hydraulic parameter than those of porous media as the porosity and permeability are developed due to secondary processes. The secondary porosity in form of fractures and weathering, introduces much more spatial heterogeneity. So it's difficult to infer the subsurface characteristics based on limited data. The aim of this research was to improve groundwater flow model of Sardon granitic catchment by determining additional model input data using hydrogeophysics. This included: i) Estimation of the spatially distributed water table depth using ground penetrating radar (GPR); ii) Characterizing the hydrostratigraphic layers using electrical resistivity tomography (ERT) in combination with previous VES data; iii) Determining a spatially distributed hydraulic parameters (transmissivity and storativity) using magnetic resonance sounding. To achieve the objective intensive field work of GPR, ERT and MRS was conducted.

GPR was implemented for estimation of the water table depths. The survey was conducted with a 200 MHz antenna combined with a differential GPS and a survey wheel for accurate positioning. Measurements were performed following a total of 35 transects (around 22.7km). The interpretation was aided by a forward GPR modelling and measured dielectric permittivity using Hydraprobe. The GPR estimated water table depths ranges from 1.32 to 2.75 m with accuracy of centimetres as compared to the measurements of water table depths in the existing piezometers.

The sub surface characterization of the catchment was performed using 13 ERT surveys and previous VES data. Based on this, the hydrostratigaphic layers of the catchment were characterized as a top high resistivity unconsolidated soil layer underlain by a low resistivity weathered and fractured granite which in turn is underlain by high resistivity massive granite. However, the thicknesses of these layers vary from place to place. The thickness of the weathered and fractured granite is higher around the Sardon stream due to the prevailing regional fault. The MRS result also confirms the existence of a high thickness aquifer around the Sardon fault.

Finally, the existing steady state groundwater flow model of the Sardon catchment was recalibrated using 22 GPR estimated water table depths, ERT and VES modified hydrostratigraphic layers and MRS derived hydraulic conductivity. The improvement as compared to the previous model was related to additional model constrain by 22 GPR estimated hydraulic heads, to readjustment of hydrostratigraphy based on 80 ERT and VES points and to improvement of the flow domain based on the newly acquired, MRS hydraulic conductivity.

Acknowledgements

A great thank to Allah; the Almighty, who has made it possible for me to complete my MSc study. I own Him many thanks for all his blessings on me.

I would like to express my sincere gratitude towards the Netherlands Government for providing me a scholarship through Netherlands Fellowship Programme (NFP) to follow this Master of Science programme at ITC.

I am very grateful to my supervisors; Dr. Ir. Maciek Lubzinyski and Dr. Mark van der Meijde for their guidance, constructive criticism and comments during the course of this Research.

I wish to record my deep gratitude to my Advisor Alain Pascal Francis who gave me immense help and encouragement from the early stage till the end of this research. I will forever be grateful for his advice, hard working approach, commitment and kindness.

I wish to extend my sincere gratitude to Mr. Siavash and Prof. Sabastian Lambort, University Catholique de Louvain, Belgium for providing GPR equipment and also for their support in the GPR interpretation. Moreover, Mr. Siavash deserves special thanks for providing GPR interpretation Codes and also for his hospitability during my Belgium travel on GPR case. I am also thankful to Mr.Arno Mulder and Mr. Alber Hemstede, TUDelft University for providing ERT equipment. I am also grateful to Dr. Jean Roy for his support in the magnetometer and MRS survey.

My heart felt thanks again goes to Alain Pascal Francis for his help during the tiresome geophysical field work and also to my friend Ermias for his help and companionship during the entire field work. I can not end with out appreciating all the Spain Sardon Field work Team who made my stay in Spain memorable.

Finally, my profound gratitude to all ITC's WREM staff and my colleagues, who by one way or the other contributed to this Research. I am indeed grateful for all the advice, comments and suggestions from you all.

Table of contents

Contents

List of figures

List of tables

1. Introduction

Groundwater continues to serve as a reliable source of water for a variety of purposes including industrial, domestic and irrigation uses. Accurate evaluation and quantification of groundwater resources is essential for sustainable groundwater management. Groundwater modelling is an optimal and well recognized tool to evaluate the groundwater flow and quantifying the potential. It also helps for understanding and predicting the behaviour of the groundwater system in response to future stresses due to abstraction or meteorological forcing. A mathematical model simulates groundwater flow indirectly by means of governing equations which represent the physical process that occur in the system together, with equations that describe the head or flow along the boundaries of the model (Anderson and Woessner, 1992).

Applications of groundwater models require extensive field information for input data and for calibration. These data can be collected by direct measurement from piezometers and wells situated in the area or by indirect measurement using hydro-geophysics. Hydro-geophysics complements direct characterization data by providing a denser grid of subsurface measurements than is obtainable from core point measurements or from volume-averaged pump test measurements alone. Geophysical data can be collected in a non-invasive manner and can be used to reduce the number of direct measurements needed to fully characterize a site (Hubbard and Rubin, 2000).

The Sardon catchment is located in the central-western part of Spain in the Salamanca province comprising 80 km^2 areas. Several research activities have been conducted in the Sardon catchment focusing on assessing and evaluating the groundwater of the area through numerical modeling approach, (Cornejo, 2000, Duah, 1999, Shakya, 2001). Subsequent to this, a lot of research works have been done to improve the reliability of the model by determining the spatio-temporal variability of fluxes (Lubczynski and Gurwin, 2005) and very recently by (Ruwan 2009). This research work is another step forward in the groundwater modeling of the Sardon catchment aiming at improving the models by determining spatially distributed hydraulic parameters using hydro-geophysics. In this research, hydro-geophysical methods like ground penetrating radar, electrical resistivity tomography and also magnetic resonance sounding were implemented. In line with this, the earlier developed steady state ground water flow model was modified and calibrated using the hydraulic parameters derived from the hydro-geophysics.

1.1. Research setup

1.1.1. Problem statement

Understanding groundwater flow behaviour is always uncertain. The non-uniqueness of groundwater model solution is due to various combinations between hydraulic parameters and fluxes (Lubczynski and Gurwin, 2005). Applications of groundwater models require extensive field information for input data and for calibration. For this, a nest of piezometers is used to estimate ground-water flow direction, flow velocities, and the location of discharge and recharge areas (Freeze and Cherry, 1979., Richardson, et al., 1992). However, the number of piezometers in the study area are limited and situated to the central part of the catchment along the Sardon river and hence, in the previous models hydraulic head for the more extensive areas among the piezometers was estimated by interpolation (Ruwan 2009). But as the area is dominated by geological structures and heterogeneity of the top layer (Tesfai 2000), the hydraulic head is more difficult to infer. Hence the ability to adequately estimate the spatially distributed hydraulic head is strongly dependent on the availability and distribution of low cost field measurements like geophysics.
In line with this, in the previous model since there was no pump test data in the area, the hydraulic parameter like conductivity and storativity were estimated from laboratory analysis of soil samples and their spatial distribution was determined using a GIS based cross overlay procedure (Lubczynski and Gurwin, 2005) .And hence, for a better estimation of the spatially distributed hydraulic parameter magnetic resonance sounding will be used.

1.1.2. Objective

The main objective of the research is to improve groundwater flow model of Sardon catchment by determining additional model input data using hydro geophysics.
The specific objectives are:-

- Estimation of the spatially distributed water table depth using ground penetrating radar (GPR).
- Characterizing the hydrostratigraphic layers using electrical resistivity tomography (ERT) in combination with existing VES.
- Determining a spatially distributed hydraulic parameters (transmissivity and storativity) using magnetic resonance sounding.
- Modifying and calibrating the steady state groundwater flow model using GPR estimated water table depths, modified hydrostratigarphy with ERT and MRS –derived hydraulic parameters.

1.1.3. Research Question

- How accurate is estimation of water table depth using ground penetrating radar?

- How good is the ERT contribution in aquifer characterization and in distributed groundwater modelling?
- What is the optimal way of using magnetic resonance sounding as input data provider for numerical groundwater model?
- What is the benefit of using hydrogeophysical techniques as input data providers in groundwater flow modelling?

1.1.4. Research Hypothesis

- Hydro-geophysical data can give a reliable estimation of hydraulic parameters of the sub surface.

1.2. Description of the study area

1.2.1. Location and accessibility

The Sardon catchment is located in the central-western part of Spain about 50 km west of Salamanca city. It is bounded between the geographical co-ordinates of 6°07'- 6°13' W longitudes and 41°01' - 41° 08' N latitudes. The catchment is part of the Rio Tormes river basin and it covers an area of about 80km^2.

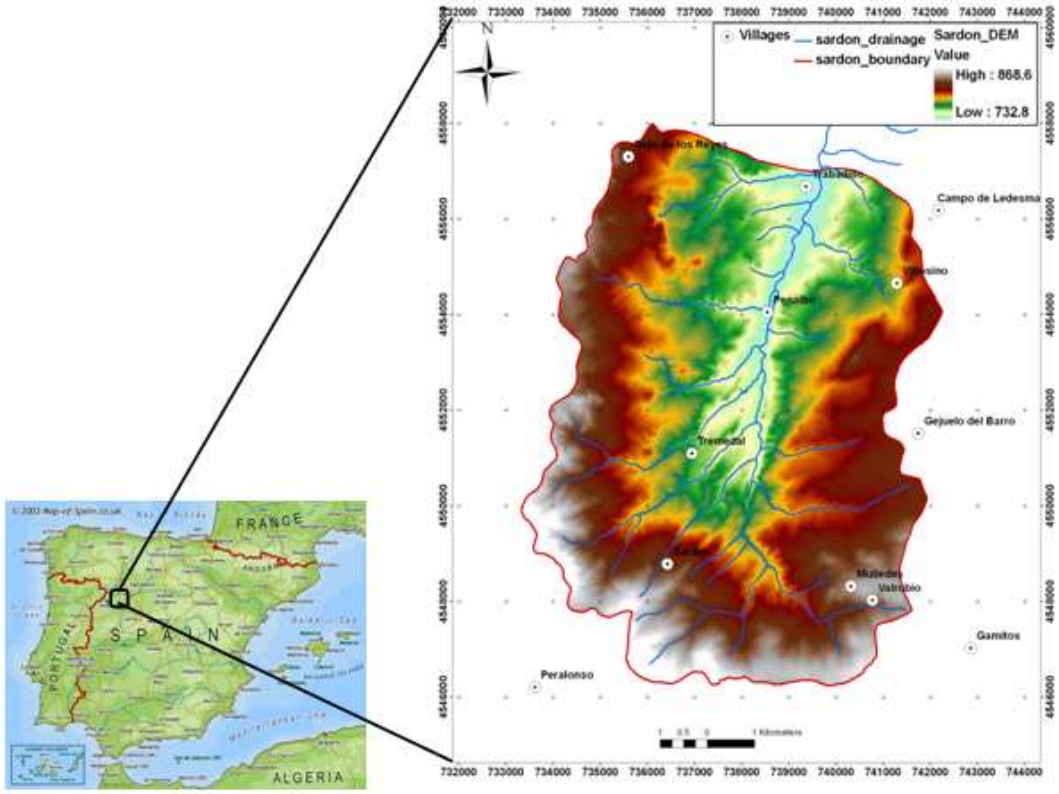

Figure 1-1: Location map of the study area

1.2.2. Climate and hydrology

The area is semi-arid and the rainfall in the surrounding catchment analysed by Duah (1999) for a period of 1962 to 1996 indicate mean of approximately 480 mm/yr. The warmest & driest months, July & August, have average temperatures of 22^0 C, a potential evapotranspiration (PET) of 5 mm/d and an average rainfall of 20 mm/month. The wettest months, November & December, have an average temperature 5^0C, potential evapotranspiration of 0.5 mm/d with 100 mm of monthly rainfall.

The Sardon river serves as a major drainage channel in the catchment where small tributaries flow towards it. The dense drainage network is largely influenced by the perennial Sardon River, which joins the big Tormes River. The Sardon River is mostly dry from June to October. However, during the wet period the flow occurs as direct runoff in response to high intense rainfall showers due the thin, highly permeable upper unconsolidated layer with low retention capacity (Shakya, 2001).

The groundwater flow pattern follows the regional Sardon fault zone in the area. Geomorphologically, the area shows two distinct units, gently undulating western part and steeper undulating eastern part, the two divided by the Sardon regional fault (Attanayake, 1999).

1.2.3. Geomorphology and land cover

The study area is characterized by a gentle undulating topography mainly controlled by geological structure and subsequent interactive weathering processes. The clearly observable series of ridges and valleys in the area testify the existence of weathering along weak structural lineament or intense joint network systems. The depression valleys possess higher thickness of alluvial and colluvial materials. The elevation varies within 732- 869 meters above mean sea level and the highest level is reported at southern boundary of the catchment. The morphology of the catchment seems to be largely controlled by the Sardon brittle shear zone (Tesfai, 2000).

The Sardon area is characterized by natural vegetation of mainly two tree species, *Quercus pyrenaica* and *Quercus ilex*. These are sparsely distributed and remaining land is covered by *Cytisus scoparius* shrub and short grass in the area. As most part of the top soil is weathered rock, agricultural practises are rare in the area. These land areas are covered by grass and weed typical in semi-arid savannah areas (Shakya, 2001).

1.2.4. Geology, structure and Soil

The study area is in the Central Iberian Zone (CIZ) of the Iberian Massif in Moncorvo-Vitigudino metamorphic belt. The Iberian Massif is generally underlain by granitic rocks belongs to the CIZ with intrusions of quartz dykes (Lopez and Carnicero, 1987). The major lithological units identified are megacrystic granite, microgranite and two varieties of mica rich granites (Attanayake, 1999). The area consists of massive granite with intermittent highly fractured and weathered granitic areas. The thickness of this weathered granite zone vary from place to place.

In a regional scale the structure is characterised by sub-vertical foliation that curves parallel to the pluton margin. The axes of the major folds are oriented in NW-SE direction with several ductile shear zones. A NNE-SSW trending system of faults, which is persistent throughout the region, completes the structural framework. The study area falls closure to the southern margin of the pluton and reflects these structures in a local scale. Such structures are observed along the Sardon River resulting subsurface flow though this shear zone (Attanayake, 1999).

.

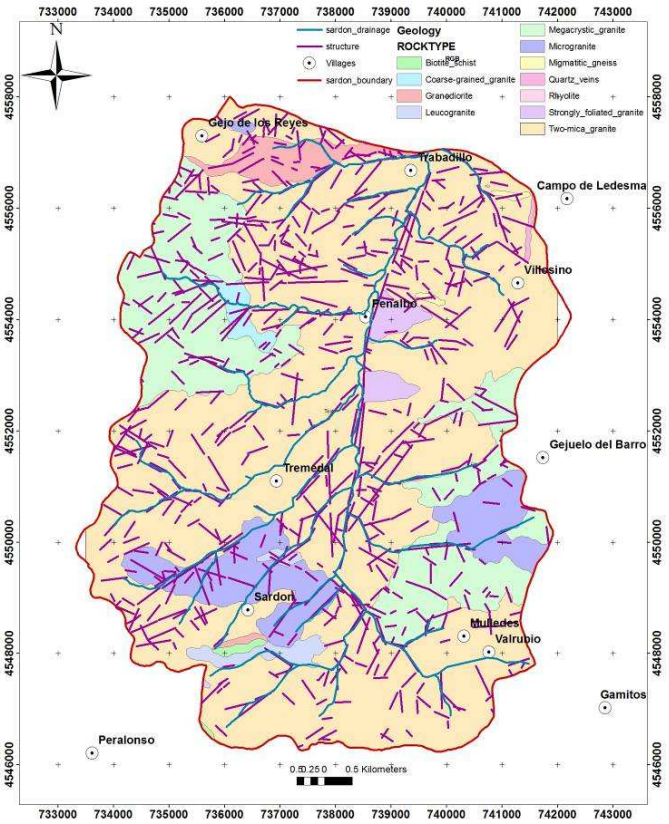

Figure 1-2 Geological and structural map of the study area (after Attanayake (1999))

1.2.5. Monitoring network

As being a research site of ITC for several years the Sardon catchment is equipped with an automated monitoring network. The network includes meteorological ADAS station and automated monitoring loggers for measuring hydraulic head variation, soil moisture and chloride content. The two automatic data stations ADAS, which are situated in Trabadillo and Muelledes since 1997, are capable of recording rainfall, wind speed, temperature, relative humidity and solar radiation data in hourly basis. The automated monitoring loggers installed at about 23 piezometers are also capable of measuring the hydraulic head and the chloride concentration in hourly basis.

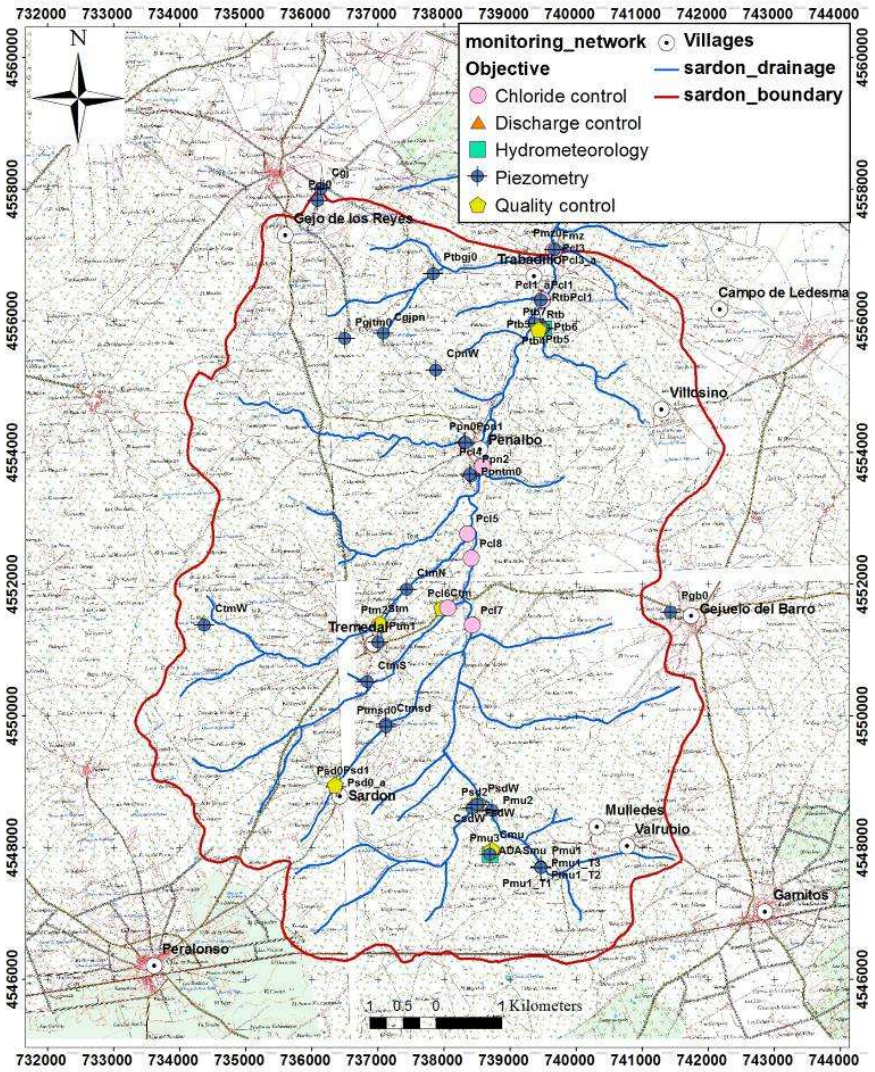

Figure 1-3: Monitoring network of Sardon catchment

1.3. Literature review

In the Sardon catchment several ITC research activities have been carried out since 1996. Some of the previous studies were focused on geology and structure of the catchment (Attanayake, 1999, Tesfai 2000). The subsurface structure and characterization of the Sardon granitic basement was assessed by Tesfai (2000) using electrical resistivity. He reported that the top most soil layer, which varies in thickness from 0.0 to 4.0 m, is followed by weathered fractured granitic layer which is underlain by massif basement granite. The groundwater balance, geochemistry, recharge and evapotranspiration of the area was assessed. (Cornejo, 2000, Shakya, 2001). In previous groundwater balance studies, spatio-temporal variability of recharge and groundwater evapotranspiration fluxes have been assessed through the combination of various techniques (Shakya, 2001). It involved the application of GIS modeling and remote sensing, sap flow measurements, chloride mass balance, well hydrograph, 1-D recharge model, geophysics and other in-situ and laboratory experiments. The various approaches such as GIS, remote sensing, automated monitoring systems, geophysics and pumping test have been integrated in a study carried in the Sardon catchment by Lubczynski and Gurwin (2005). As indicated by the authors, the calibrated model involves a spatial and temporal non-uniqueness, mainly due to uncertainty between groundwater evaporation and groundwater outflow which could not be measured. Recently Ruwan (2009) tried to improve the model reliability by upgrading the steady state flow model and later validating through solute transport model by chloride measurements and also he develop the transient flow model for the period of 2003-2008.

Ground penetrating radar (GPR) is a near-surface geophysical technique that can provide high resolution images of the dielectric properties of the top few tens of meters of the earth (Doolittle, et al., 2006). It is a time scaled system which measures the time it takes electromagnetic energy to travel from an antenna to an interface. The penetration depth of GPR is determined by antenna frequency and the electrical conductivity of the earthen materials being profiled (Daniels, 2004). Materials having high electrical conductivity rapidly attenuate radar energy, restrict penetration depths, and severely limit the effectiveness of GPR. GPR has been used extensively for hydrological investigations for over 30 years. In areas of coarse-textured soil materials, GPR has been used to estimate water-table depths among wells and into nearby areas (Doolittle, Jenkinson, Hopkins, Ulmer and Tuttle, 2006, Iivari and Doolittle, 1994, Sellmann, et al., 1983., Smith, et al., 1992). Furthermore, GPR was implemented in estimation of groundwater level in an area with multiple ambiguous reflections. In order to identify the groundwater reflection amongst a set of ambiguous reflectors and to increase the signal-to-noise ratio, the common-midpoint (CMP) method was used (Nakashima, et al., 2001). GPR and computer processing techniques was also applied to chart water table depth and assess local groundwater flow in an area having intricate soil patterns, undulating topography, and non-homogeneous or anisotropic strata (Iivari and Doolittle, 1994).

Electrical resistivity surveys have progressed from conventional vertical soundings to techniques such as ERT, which provides two and even three-dimensional high-resolution electrical images of the surface (Colella, et al., 2004). Electrical resistivity tomography (ERT) is a well established technique, both as a surface (Baker and Moore, 1998) and a cross-hole subsurface imaging (Daily, et al., 2004, Kemna, et al., 2002). ERT has been widely applied in 2D and 3D imaging of the subsurface in areas of complex geology (Griffiths and Barker, 1993). It was also implemented in tectonically active areas for delineation of structures (A. Giocoli, et al., 2008, Caputo, et al., 2003). Furthermore, ERT survey was employed to localize aquifer boundaries and design the installation of a groundwater monitoring network to constrain groundwater flow model (Mastrocicco, et al., 2009)

Magnetic resonance sounding bases on the principle of nuclei spinning of the hydrogen proton in water molecule (Kirsch, 2006). It supplies a depth wise water content characteristics that is convertible into hydro-geological parameters of saturated and unsaturated zones (Lubczynski and Roy, 2007). Hence, it is particularly adapted to hydro-geological investigations for determining hydrogeologic parameters like transmisivity and specific yield (Boucher, et al., 2009, Legchenko, et al., 2004, Roy and Lubczynski, 2003). The depth of investigation capability of MRS depends on its excitation or sensing loop, electric conductivity of the medium, ambient noise level and amount of Earths magnetic field. Being a new method, to evaluate the performance of MRS surveys several tests were conducted in various places with different geological set up(Goldman, et al., 1994).

2. Materials and Methods

The study was conducted using data obtained from previous works and from field work. The methods followed in the research process are based on the objectives formulated in section 1.1.2

2.1. Pre-field work

Prior to the field work the following tasks were carried out:

- Reviewing of literatures related to hydrogeophysical methods like ground penetrating radar, magnetic resonance sounding and electrical resistivity tomography and also about groundwater flow model. Revising various appropriate softwares like, Matlab, MODFLOW, 2D EarthImager resistivity, GPRMAX and GIS and remote sensing software as well.
- Collection and study of previous works like the already developed steady state model and various maps (geology, drainage, soil, boundary, and lineament) and also raw VES data.
- Preparation of sampling scheme for the ground penetrating radar, electrical resistivity tomography and magnetic resonance sounding survey. This was performed using GIS and remote sensing by considering the soil type, geological structures and the measurements from the existing piezometers.
- Proposal writing
- Preparation of work plan for the field work

2.2. Field work

During the field trip, which was carried out from August 31 to September 29, the following tasks were performed:-

- Meteorological and hydraulic head data were downloaded from Automatic data acquisition system (ADAS) and monitoring loggers respectively.
- Electrical resistivity tomography survey was performed for determination of the hydrostaratigraphic unit.
- Ground penetrating radar survey was conducted using a 200 MHz antenna for estimation of the water levels. The survey was aided by DGPS for accurate positioning. Moreover, to improve the interpretation of GPR, dielectric permittivity of soils and rock were measured using HydaraProbe.
- Magnetic resonance sounding survey was also conducted for determining the hydraulic parameter. Prior to this MRS survey, magnetometer survey was conducted for identifying magnetic anomaly since MRS has low signal or even fails in high magnetic gradient environment. The magnetic resonance sounding survey was conducted in October 2009 by Alain Pascal Francis and Jean Roy based on the predefined sampling scheme.

2.2.1. Post field work

At this stage, the data collected during the pre field and fieldwork were processed and analyzed. The main tasks in this stage were:

- The ERT data were inverted using AGI 2D EarthImager resistivity software.
- The previous VES data were also inverted using one dimensional resistivity software (IPI2 win (lite)).
- The hydrostartigraphic layers were developed by interpolating the ERT-VES derived thickness using KED (kriging with external drift) method in R_geostatistical environment.
- The radar profile obtained from the GPR investigation was converted into water table depth using a Matlab based code developed by Siavash. This interpretation is aided by forward GPR model developed using GPRMAX software.
- Inversion of the magnetic resonance sounding profile in to hydraulic parameters using NUMIS software. Interpretation was done based on standards from previous studies since there is no pumping test data for the area.
- The steady state model was calibrated using the GPR estimated groundwater table and MRS derived hydraulic parameters. For this MODFLOW software with PMWIN 5.3 interface was used. The calibration process was conducted using trial and error and through automated parameter estimation (PEST). The results of the calibration should be evaluated both qualitatively and quantitatively (Anderson and Woessner, 1992). Hence, calibration error of the model was quantified.

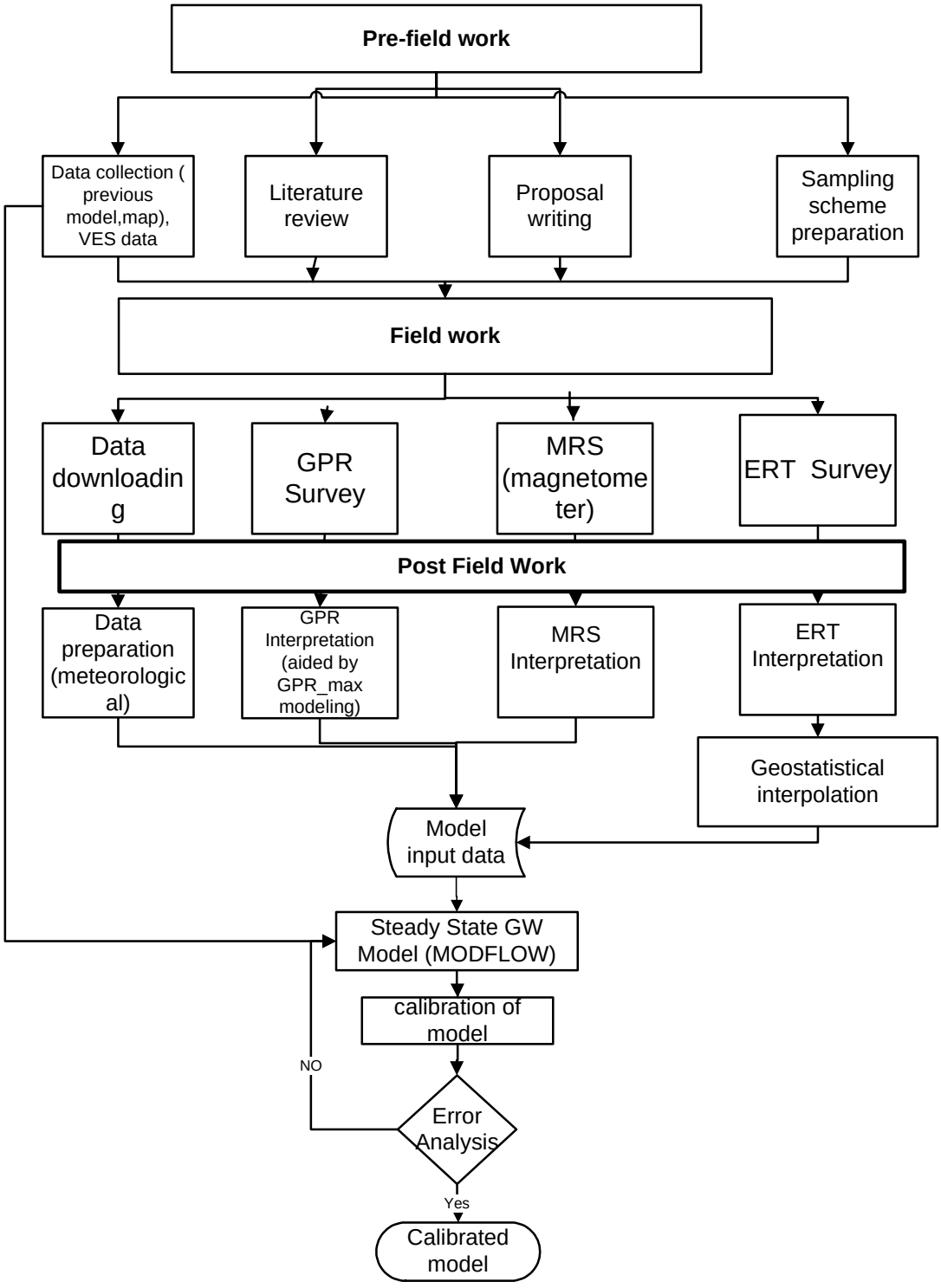

Figure 2-1 Flow chart of activities

2.3. Ground penetrating radar

2.3.1. General principle

When transmitted electromagnetic signal enters the ground, it contacts objects or subsurface strata with different electrical conductivities and dielectric constants. Due to a change in the bulk electrical properties of different subsurface lithologies, mineralogy, and/or the character of the sediment interface, some of the energy is reflected back to the surface (Davis and Annan, 1989). At the surface, a receiver monitors reflected energy versus delay time. The pulse delay time from the energy transmitted into the ground and reflected back to the receiver, is a function of the EM propagation velocity through the sediment and the depth of subsurface reflectors. Strength of the reflected signal is approximately proportional to the difference in dielectric constants at the sediment interface (Davis and Annan, 1989). These effects enable the subsurface stratigraphy and structure to be inferred from the character of the radar return signals. GPR provides a profile of horizontal survey distance (m) versus vertical two-way travel time in nanoseconds (1ns=10^{-9} seconds). By measuring the propagation velocity of sediment, the two way travel time can be converted to depth of reflections using the two basic equations (Daniels, 2004) :

$$d = \frac{tV}{2} \quad (1)$$

And $$V = \frac{C}{\sqrt{\varepsilon_r}} \quad (2)$$

Where d=depth in meter; t=two way travel time in nanoseconds; C=velocity of light in free space in meter per nanosecond; ε_r =relative dielectric permittivity a dimension less; and V= electromagnetic wave velocity in meter per nanosecond.

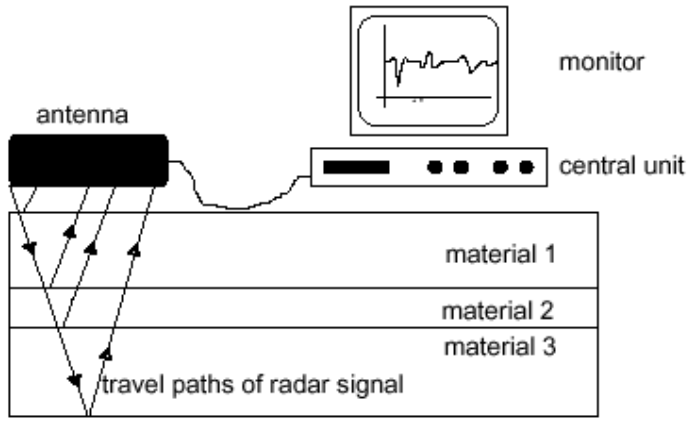

Figure 2-2 Illustration of GPR Operation

Changes in the dielectric constant and electrical conductivity can also affect the rate of energy attenuation. Since fine-grained sediments such as silts and clays, which have high conductivities, cause high signal attenuation and reduce the penetration depth to a few meters or less, GPR is limited to environments of low conductivity (Annan, 2002).

2.3.2. Pre-processing of GPR data

Since in most cases the subsurface geology is complex, interpretation of GPR data needs to be pre-processed to enhance the part of the data related the reflection from the target. The common effects that have to be removed in pre-processing stage of GPR data interpretation are noise, common clutter, and path loss. These undesired effects are discussed below:

Path loss compensation

Due to the path loss both by the ground conductivity and by the spreading effect, the received signal is attenuated when compared with the transmitted one. This attenuation depends on the range of the reflector (r). If the reflector is flat enough in comparison with the wave length the spreading loss is in proportion to 1/r. Otherwise it is proportional to $1/r^2$ (Daniels, 2004).The medium ground loss is given by

$$\text{Loss}= e^{2\alpha r},\ \alpha = \omega\sqrt{\frac{\mu\varepsilon}{2}\left[\sqrt{1+\left(\frac{\sigma}{\omega\varepsilon}\right)^2}-1\right]} \qquad (3)$$

Where σ , ε and μ are the conductivity , permittivity and permeability of the medium respectively and α is the attenuation constant ω

Path loss is compensated by applying a time variable gain (range gain). The gain in decibel is selected as a piecewise linear function of time. Assuming that the two way travel time relates to *r* through a constant value, this selection can be justified by deriving loss in decibel

$$\text{Loss (dB)} = 20\ \log 10\ \text{loss}=17.372\,\alpha r \qquad (4)$$

Background removal

Those reflections that are not related to the target scattering characteristics but have similar spectral features to the target echo are regarded as clutter. Clutter is defined as the reflections that occur in the same time window of several scans. Eg. The surface reflection, antenna ringing and the echoes form the subsurface planer interfaces. Background removal eliminates clutter in GPR data. Background removal is attained by dividing the radar gram in to vertical strips. Taking an average of the scans across each strip and subtracting the average from each scan of the strip. The width of each strip is specified in terms of the relative location of the targets to each other. As a rule of thumb, the width for all strips is equally set to the number of scans of the largest target (Daniels, 2004).

Averaging and filtering

Averaging is one of the techniques used to eliminate the effect of the noise. The average of a number of radar signal taken at a single point on the ground is considered as the received waveform for the point. Viewing the noise as additive white Gaussian noise, it can be shown that averaging N radar signals improves signal to noise ratio (SNR) N times. Another method to improve SNR is low pass filtering in which high frequency noise especially visible in the lower portion of the radargram is removed.

2.3.3. GPR forward Modelling

GprMax2D is electromagnetic wave simulators for Ground Penetrating Radar modelling. It uses a Finite-Difference Time-Domain numerical method to numerically solve the well known Maxwell's equations which are the governing equations in GPR system;

$$\nabla \times \mathrm{H} = \sigma \mathrm{E} + i\omega\varepsilon \mathrm{E} \quad (5)$$

$$\nabla \times \mathrm{E} = -i\omega\mu \mathrm{H} \quad (6)$$

Where $\mathrm{i} = \sqrt{-1}$, ω is angular frequency, ε, σ and μ are the dielectric permittivity, magnetic permeability and electric conductivity parameters and E and H are the electric and magnetic field vectors.

In order to simulate the GPR response from a particular target or set of targets the above equations have to be solved subject to the geometry of the problem and the initial conditions. GPR max2D needs a set of parameters as an input including dielectric permittivity, electric conductivity, model geometry (number of layers, layer thickness, and length of model) and frequency. It then gives the simulated GPR signal as a two way travel time in seconds versus distance like that of the GPR (@www.gprmax.org).

2.3.4. Data acquisition and processing

The GPR data were collected using a Subsurface Interface Radar SIRveyor SIR-20 manufactured by Geophysical Survey Systems, Inc. (GSSI). SIRveyor SIR-20 is a multi channel, general-purpose, ground penetrating radar system that digitally records the GPR profiles on a hard drive.

This SIR-20 GPR was combined with a single 200 MHz bowtie antenna equipped with a survey wheel and a differential GPS for accurate positioning .During the survey the antenna was towed at the end of around 13m rope behind a four-wheel drive car (figure 2:4) which contain the main unit inside. The separation between the antenna and the towing car ensured the reflections of the car did not interfere with subsurface reflection. Because of the wide separation between the car and the antenna, it was necessary for the antenna to be manually turned around corners and obstacles. The survey was conducted following A total of 35 transects (*Figure*

2.3) of which some traverses passed as close as possible to existing piezometers and ponds to calibrate the GPR profile with existing depth of water table. The total length of the transects was 22.7km. In line with this the dielectric permittivity of some materials was measured using Hydraprobe (Fig.2-5) to aid the interpretation. The measurement of the dielectric permittivity was done not only surficially but also in sub-surface by digging holes and by drilling boreholes with Cobra equipment.

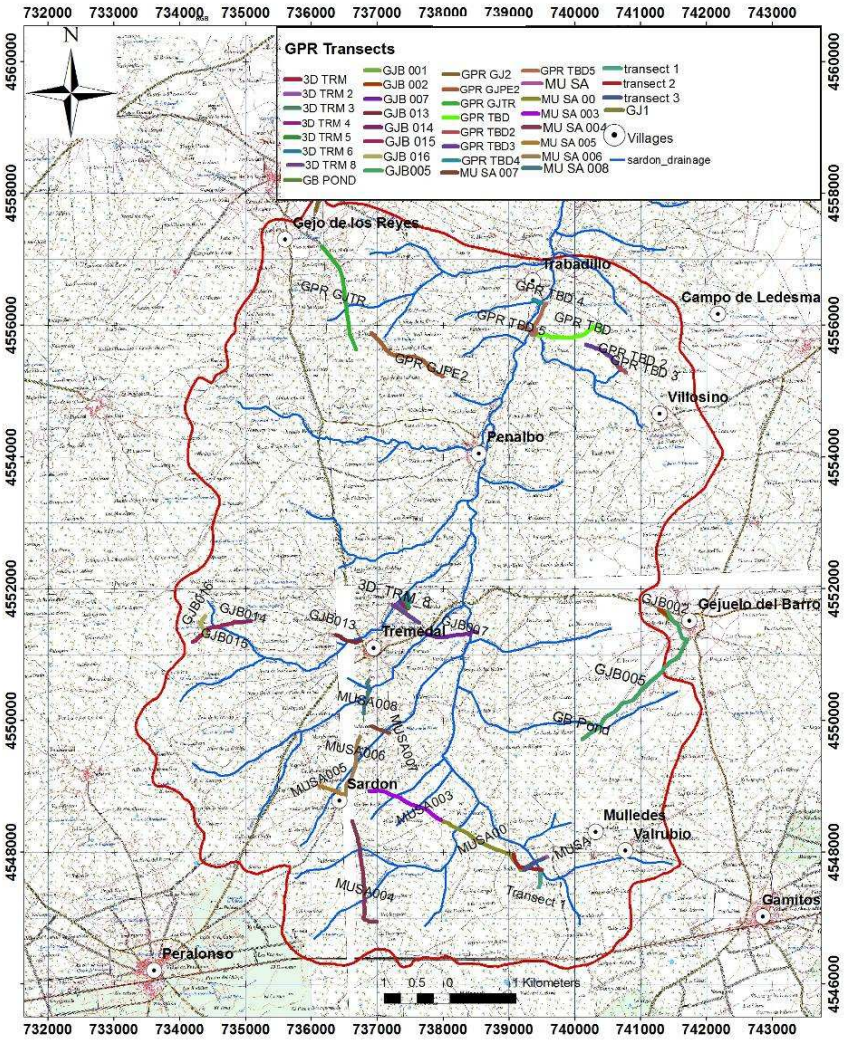

Figure 2-3: GPR Transects with monitoring network

All the GPR survey points were accompanied by differential DGPS for accurate positioning. The DGPS was mounted on the towing car (Figure 2.4) so as to avoid reflection interference. After the survey the gap between the DGPS and GPR antenna was corrected using the common trigonometric formulas. The corrected position was checked by overlaying with 5meter resolution ortho photo.

The GPR profiles were interpreted using a Matlab based code developed by Mr. Siavash (University catholique de Louvain, Belgium). The code implements all the pre-processing techniques that are mentioned in section 2.3.1. In addition the Siavash's code is capable of removing the topographic effect using the DGPS acquired positions. The code was also capable of converting the two way travel time into depth. However, since the code is designed for different type of antenna than the one used in this study, automatic inversion was not applied. Hence, for this study the conversion of arrival time to depth was performed manually using equation 1 and 2.

Figure 2-4: photo showing the GPR survey

Figure 2-5: Photo in applying Hydra Probe

All the GPR profile raw data have passed through the pre-processing step. After that, the discrimination of water table was done aided by forward GPR model. Depending on the occurrence of water table in the study area forward model was developed using GPR max 2D software. The final conversion of arrival time to depth was applied only to some selected profiles since the manual conversion using equation 1 and 2 is time taking.

2.4. Electrical resistivity tomography

2.4.1. General principle

The purpose of electrical resistivity surveys is to determine the subsurface resistivity distribution by making measurements on the ground surface. From these measurements, the apparent resistivity of the subsurface can be estimated. The ground resistivity is related to various geological parameters such as the mineral and fluid content, porosity and degree of water saturation in the rock (Griffiths and King, 1981) .By measuring the electrical potential difference induced by an electrical current passing through a material, the resistance of that material can be calculated. Measured current and voltage together with electrode geometry could be converted in to apparent resistivity. The governing equation for resistivity survey is:

$$\rho = \frac{K * \Delta V}{I} \qquad (7)$$

ρ _Apparent resistivity

ΔV _Potential difference

I _ Current

K _Geometric factor

Though the above principle holds true for both 1 D and 2D resistivity survey, the number of electrodes in 1D survey is 4 whereas in 2D ERT survey a series of electrodes could be used (Figure 2.6)

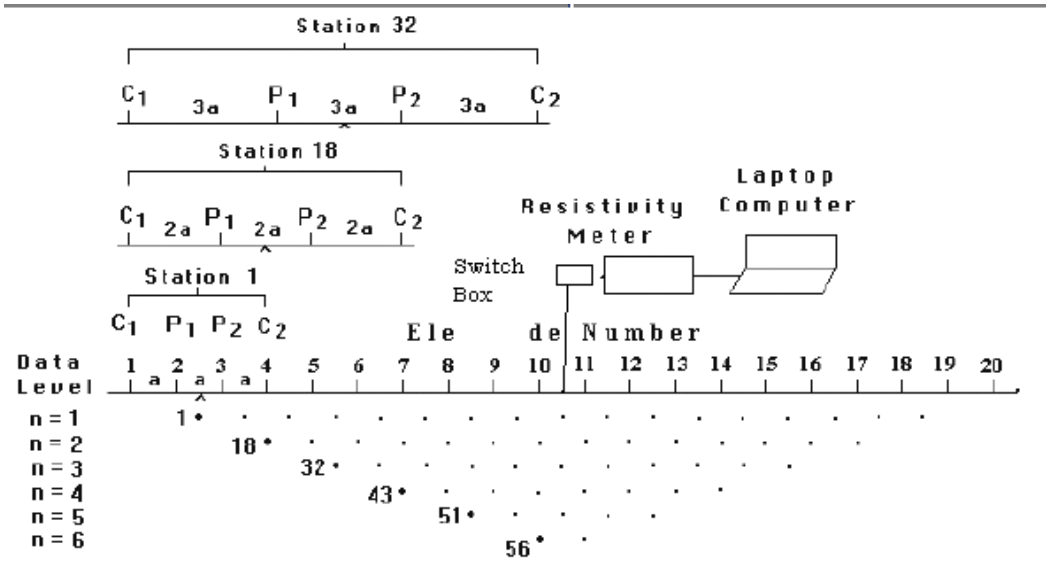

Figure 2-6: illustration of ERT operation

Automated data collection allows hundreds of individual measurements to be made in a matter of hours while minimizing the manual labour previously needed for resistivity fieldwork. Commercially available inversion software for personal computers and advances in computer hardware have allowed for rapid processing and inversion of apparent resistivity field data and for creation of two-dimensional resistivity earth models of the subsurface. Several data collection schemes are available for subsurface resistivity studies. Each of these techniques take a series of voltage and current measurements from an array of electrodes placed on the ground surface along a line of profile (Seaton and Burbey, 2002). The acquisition can be carried out using diverse electrode configurations (e.g., Dipole–Dipole, Wenner, and Schlumberger) that are positioned on a surface in order to inject the electric currents into the ground and measure the voltage signals generated. The apparent electrical resistivity is then calculated using a predetermined geometrical constant for the device employed.

2.4.2. Data acquisition and processing

The ERT data were acquired using an Advanced Geosciences, Inc. (AGI) Super Sting R8 resistivity instrument. The unit is a DC-powered, battery operated, automatic; eight channel resistivity and IP system. This system employs the SuperSting Swift general purpose cables that can be attached in series. Each cable segment contains fourteen electrodes. Each electrode has the capability of acting as either a current transmitter or as potential measuring receiver. A total of 56 electrodes were used in this survey of which some electrodes were not functional (*Table 9, annex*). In order to have a better vertical resolution the Schlumberger and Inverse Schlumberger configuration were implemented with an electrode spacing of 3m for most sites and 5m at places across the streams. A total of 13 surveys were conducted *(Figure 2.6).*

Profiles with 3m electrode spacing reaches to a depth of around 30m and array length of 165m whereas, profiles with 5m electrode spacing reach to a depth of 50m and an array length of 275. The inversion of all the ERT profiles was done using AGI resistivity 2D earth imagery software. To have a better inversion result, noisy data which might be associated with the non-functional electrode used in data acquisition were removed during the inversion. Terrain correction was also applied for some profiles which were conducted in areas with significant topographic variation. Further more, smooth inversion method was used for all profiles as it is recommended for noisy data inversion (AGI EarthImager 2D manual). Hence, most of the profiles were inverted with a minimum RMS error and Norm.

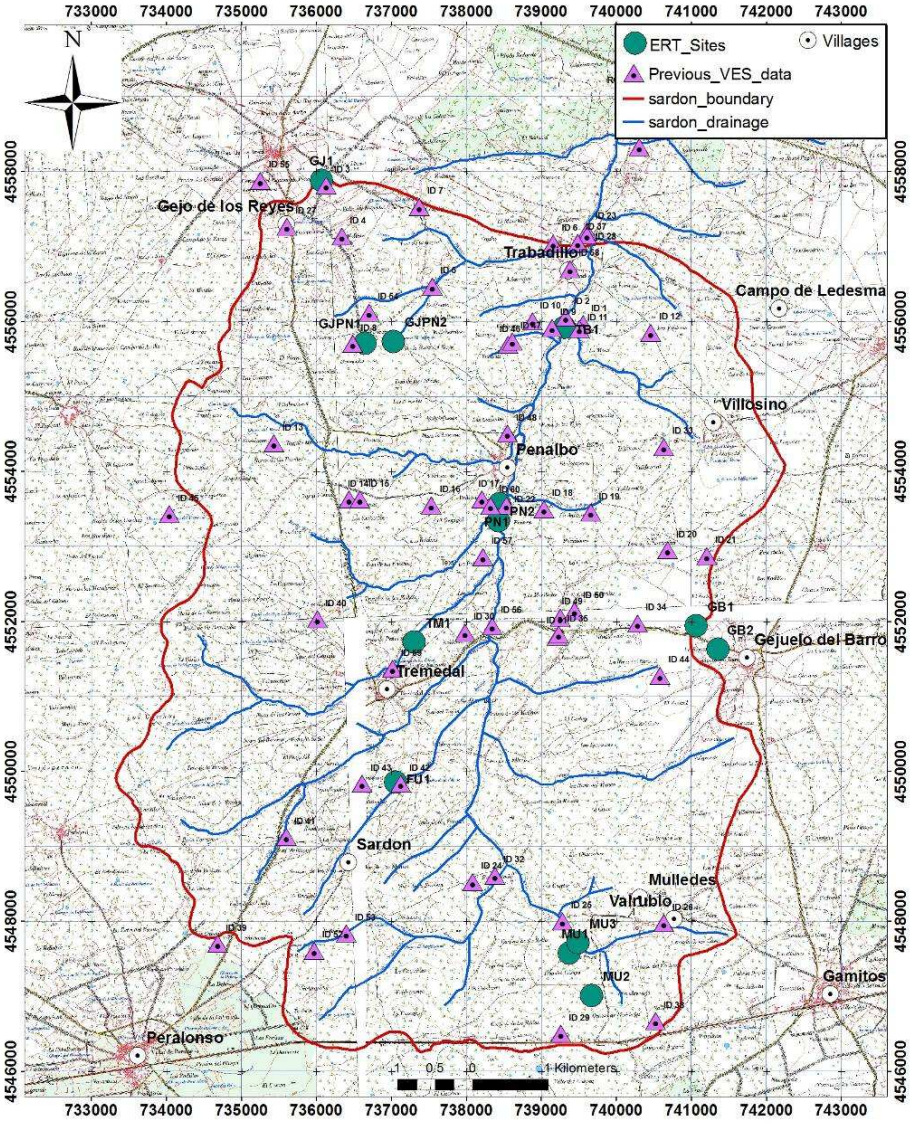

Figure 2-7: ERT and Previous VES sites with monitoring networks

2.5. VES data

The VES data which were collected from previous works are included in this research. The VES survey was conducted using ABEM SAS-300 terrameter with Schlumberger array arrangement of maximum AB/2 distance of 200m (Tesfai 2000). 50 raw VES data were obtained and re-interpreted using IPI2 WIN (lite) software (Moscow State University Geophysical department, Russia). These data together with the ERT data of this study are used for characterization of the hydro-stratigraphic unit.

2.6. Magnetic resonance sounding

2.6.1. General principle

The operating principle of the MRS is based on the excitation of protons in subsurface water in the Earth's magnetic field. The instrument consists of transmitter and receiver units. The transmitter drives an alternating current at the resonance frequency through the wire loop laid on the Earth's surface. The current is abruptly terminated and the MRS signal is then measured using the same wire loop as the receiving antenna. This procedure is repeated from several tens to a few hundred times, during which the MRS signal is recorded and averaged to improve the signal- to-noise ratio. The signal is then interpreted in terms of hydrological parameters as a function of depth using an especially developed inversion program. In magnetic resonance sounding method, a circular or rectangular wire loop on the ground surface is energized by rectangular pulses of alternating current of frequency equal to that of the proton resonance in the geomagnetic field. For an excitation pulse, the time varying current in the loop is described as;

$$I(t) = I_0 \cos(\omega_0 t) \qquad (8)$$

Where t is time and I_0 is the amplitude of the input current. The angular frequency is $\omega_0 = 2\pi f_L (= \gamma H_0)\ \omega_0$, where f_L is the resonance frequency (≈ 2 kHz), H_0 is the magnitude of the geomagnetic field and γ is the gyro magnetic ratio of protons.

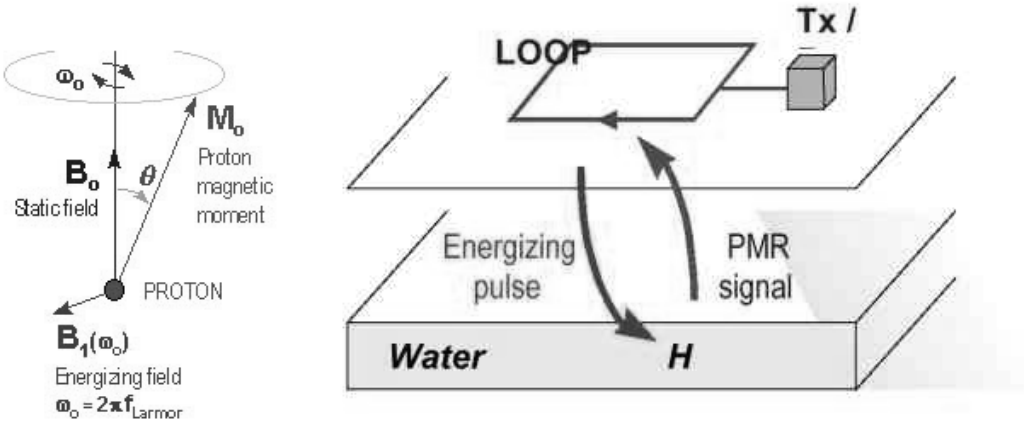

Figure 2-8 illustration of MRS operation (From (http://www.geo-hydrology.com/)

The transmitted oscillating magnetic field causes nuclear magnetization of the protons in groundwater to shift away from the equilibrium position along the geomagnetic field. When the excitation current is turned off the free Larmor precession of these protons in the earth's magnetic field causes an electromotive force (emf) to be induced in the loop. The voltage induced in the loop is an exponentially decaying function of time and is given as in *Figure* 2-9 by:

$$E(t) = E_0 \exp(-t / T_2^*) \cos(\omega_0 t + \varphi) \qquad (9)$$

where E_0 is the initial maximum voltage induced in the loop, T_2^* is the spin–spin or transverse relaxation time of water protons and is the phase shift between the input current and the induced voltage (it is zero for non-conducting rocks). The excitation pulse moment $q=I_0 t_p$ (t_p is the current pulse duration) can be varied to probe different depths resulting in a form of depth sounding. The quantities, E_0, T_2^* and φ are the interpretive data measured for various pulse intensities during depth sounding.

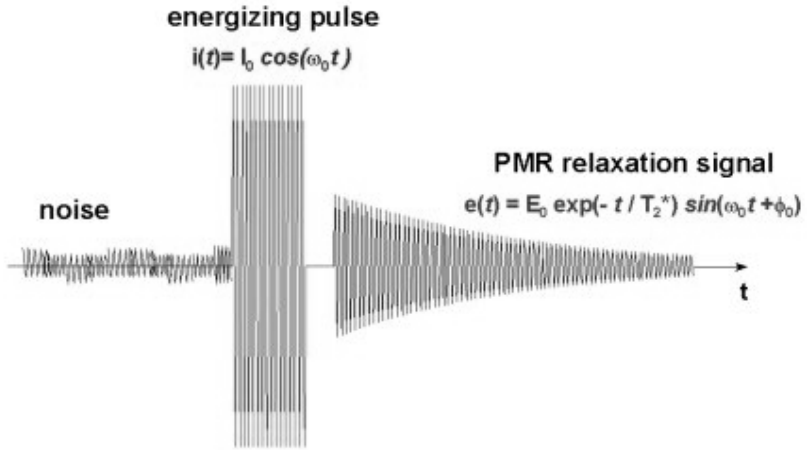

Figure 2-9: MRS Signal propagation

2.6.2. Data acquisition and processing

The MRS survey was conducted in two steps. First in September 2009, a magnetometer survey was conducted for determining the magnetic anomaly in the catchment since MRS is not working in areas of strong magnetic anomaly. The magnetometer survey was done using two hardware types. Spatial measurements were done using a magnetometer Geometrics G816 as rover and temporal measurements were taken every minute with a Geometrics G856 as base station. The measurement was conducted along a linear transect for nine sites and as a predetermined 6x6 linear grid with an interval of 20m for eleven sites *(Figure 2.10)* The magnetic field measured with the rover was corrected from the diurnal drift measured with the second hardware type, base magnetometer, by using the Geometrics software (MagMap2000). After the magnetometer survey was analysed and the magnetic anomaly in the area was confirmed to be low, the MRS survey was carried out by Alain Pascal Francis and Jean Roy from 24th October to 7th November 2009. This survey was conducted using a square loop size of 15 to 80 m. A total of 15 surveys were conducted during the field work (Frances, 2010).

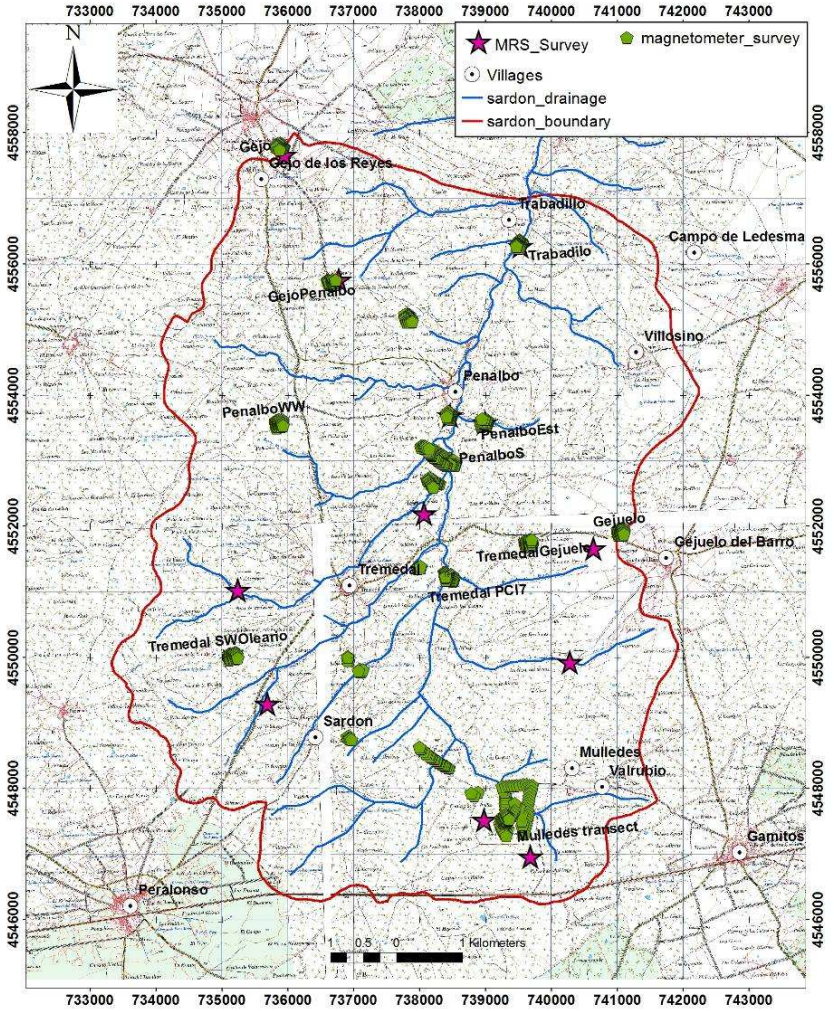

Figure 2-10: Magnetometer and MRS survey sites

2.7. Differential GPS

Every GPR, ERT and MRS survey was assisted with the differential GPS measurement. This measurement was performed by the Leica system characterized by accuracy in a range of few centimeters. For “static” objects, standard GPS survey was performed. In case of “mobile” GPR survey, the Leica GPS was mounted on car for continues positioning of the survey.

2.8. Steady state Groundwater model

The existing steady state groundwater model (Lubczynski and Gurwin, 2005)was developed using MODFLOW software. The existing model was upgraded with hydraulic heads obtained by GPR, improved hydrostratigraphy with ERT and VES and improved hydraulic flow domain with MRS. Such model was finally calibrated applying standard calibration protocol (Anderson and Woessner, 1992)

3. Result and Discussion

3.1. Determination of water table depth using GPR

GPR data needs to be pre-processed to enhance the part of data related the reflection from the target, since in most cases the subsurface geology is complex. The GPR profile before pre-processing is difficult to interpret as it is full of noisy structures. But, after pre-processing is done the reflections from the subsurface materials can be clearly seen and structures also can be observed (*Figure 3:3-3:4*).

To verify the GPR reflection and to have better understanding of differentiating the reflections from the water table, a forward GPR model was developed. The input hydroelectric sections for the forward model were obtained from ERT profiles and from direct measurement of dielectric permittivity using hydra probe (Table 2). Subsequent to this, the occurrence of the water table was generalized in two cases based on the existing wells and piezometers in the study area. The first case is when the water table is inside the soil layer (Fig. 3-1) and the second when the water table is inside the weathered granite (Fig.3-2). For the case 1, when the water table is inside the soil layer, the hydrostratigraphic layer sequence becomes as follows: unsaturated soil as a top layer, saturated soil as a middle layer (i.e. water table at the top) and saturated weathered granite as a bottom layer. For the case 2 the hydrostratigraphic sequence is as follows: unsaturated soil as a top layer, unsaturated weathered granite as middle layer and saturated weathered granite (i.e. water table at the top) as bottom layer. Note that in both cases, the bottom layer is the massive granite as it is summarized in *Table 1* but this layer is not considered in the forward modelling since the penetration depth of GPR is too shallow to reach that layer.

Table 1: Hydrostratigraphy in Sardon catchment (from shallower layer to deeper layer)

Layer	Lithology	Thickness (m)
Soil	silty sandy, low content of clay and organic matter	0.5 - 7
Weathered and fractured granite	Granite with some alteration, fractured. Contact with previous layer	4 – 35
Fresh granite		NA

The electrical parameters of these layers are showed in *Table 2* as function of the saturated or unsaturated states. Note that the terminology "unsaturated" is used here to describe a layer that is at its minimum water content.

Table 2: Parameters for the hydrolayers considered in the GPR forward modeling

Layer	Stratigraphy	Resistivity (_Ohm_m)			Conductivity (_mS_per_m)			dielectric permittivity			Thickness_m		
		min	max	value	min	max	value	min	max	value	min	max	value
SOIL_UNSAT	A	500	1500	700	0.67	2.00	1.43	3	9	5	0.0	3.0	2.0
SOIL_SAT	A1	10	100	50	10.00	100.00	20.00			25	0.0	6.0	1.0
SOILPEBBLES_UNSAT	B	200	750	500	1.33	5.00	2.00	7	9	8	0.1	0.5	0.5
SOILPEBBLES_SAT	B1	5	75	50	13.33	200.00	20.00			20	0.1	0.5	0.0
WEATHGRANITE_UNSAT	C	500	1000	800	1.00	2.00	1.25	5	15	7	0.0	2.0	1.0
WEATHGRANITE_SAT	C1	200	400	250	2.50	5.00	4.00			27	5.0	50.0	10.0
HARDGRANITE	D	1500	5000	2000	0.20	0.67	0.50			4			100.0

As it can be seen from the forward GPR simulation results the water table shows a strong reflection signal in both of the cases (Figure3.1 and 3.2) and also a multiple reflection is seen below the water table reflection. This is due to the fact that water has higher dielectric permittivity (ε =80) moreover multiple reflection is common below the water table reflection (Annan, 2005). However, the geological contact between soil and granite is not clearly seen in the forward GPR result for case one i.e. when the water table is inside the soil just above the contact. The models presented here do not consider the soil pebble layers and other heterogeneities.

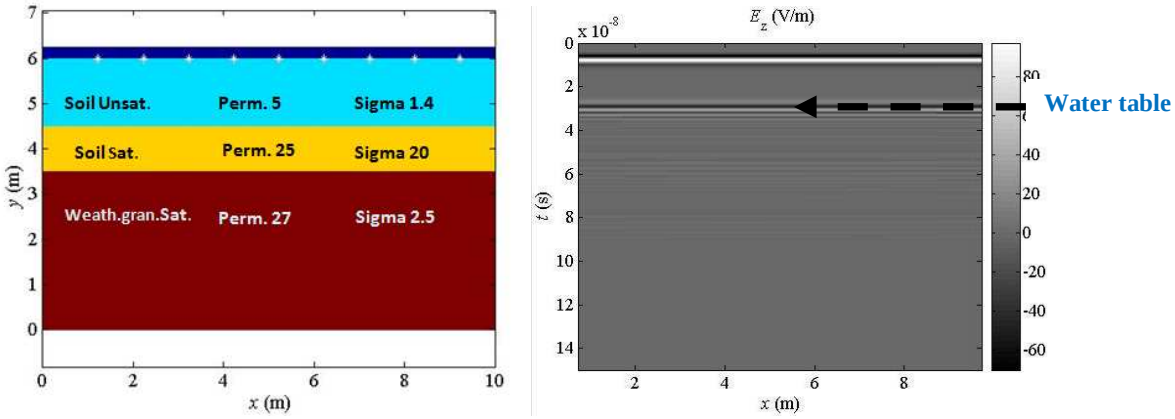

Figure 3-1: forward GPR model for case 1

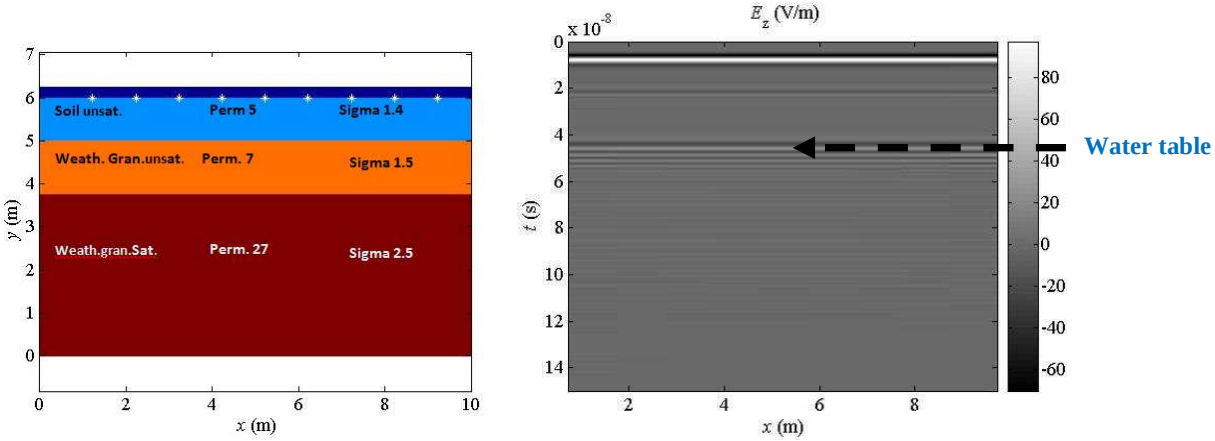

Figure 3-2: Forward GPR model for case 2

The conversion of the two ways travel time into depth depends on the speed of the material in which the signal is propagating. The speed also depends on the dielectric permittivity of the material. Hence, knowing the dielectric permittivity is the basis for conversion of the time into depth. Therefore, during the field work, dielectric permittivity of some of the materials was measured. Based on the forward GPR model the processed GPR profiles of the survey were categorized as case 1 and case 2 types. Following this, for the type 1, a dielectric permittivity 5 was used while for type 2 a dielectric permittivity of 6. In both cases, these dielectric permittivities were used for the conversion of the arrival time into depth using equations 1 and 2. Conversion of arrival time to depth was applied to selected profiles. For example as shown in Figure 3.3, the higher reflection is around t=20ns. Taking the velocity of light in free space as $C=3x10^8$ =0.3m/ns and using dielectric permittivity of 5 for type 1, results in the velocity (V) and water table depth (d) as follows:

$$\text{And } V = \frac{C}{\sqrt{\varepsilon_r}} \quad = \quad V = \frac{3x10^8}{\sqrt{5}} \quad = 0.1342\text{m/ns}$$

$$d = \frac{tV}{2} \qquad d = \frac{20x0.134}{2} = 1.34\text{m}$$

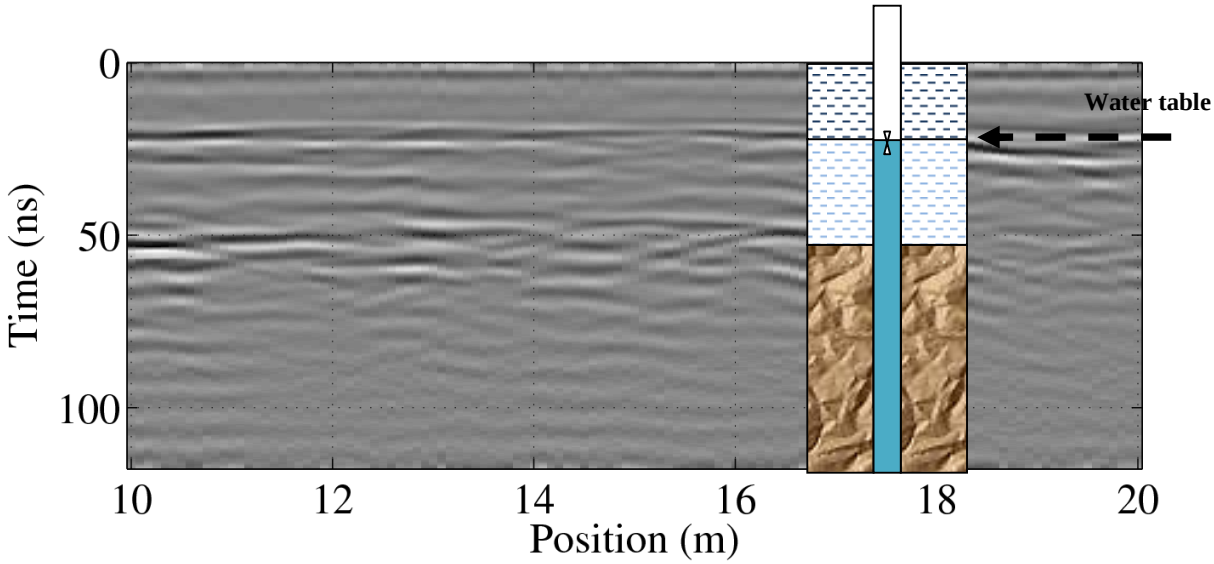

Figure 3-3: Case 1 type GPR profile (Transect around Trabadilo near the stream)

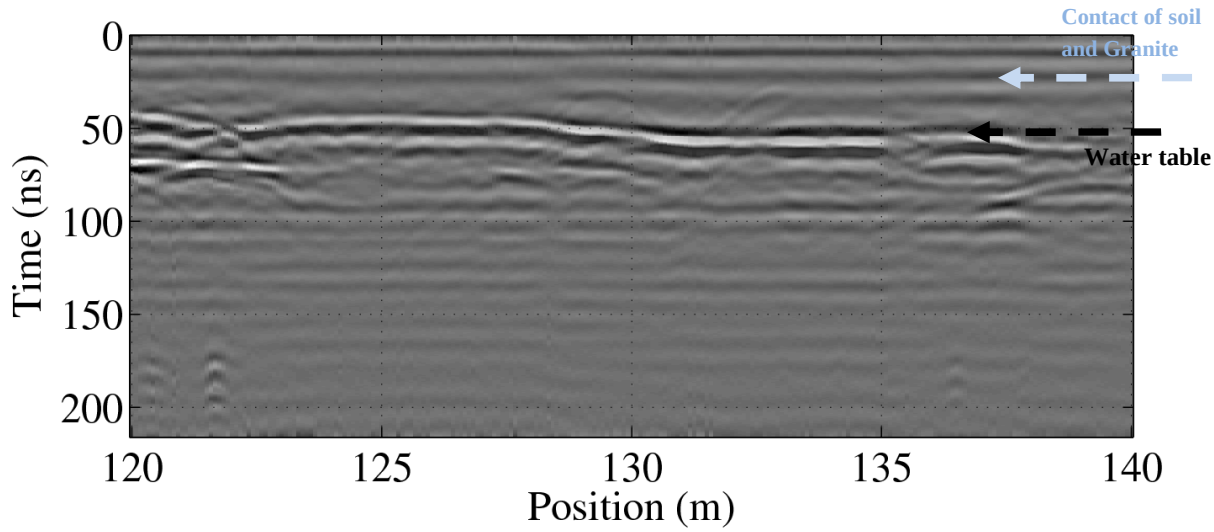

Figure 3-4: Case 2 type GPR profile (transect around mulledes Sardon)

As can be seen from *Table 3* the GPR estimated water table depths ranges from 1.34 to 2.76 meter. The maximum depth is obtained around the north eastern part of the catchment and the minimum is obtained around the Sardon River. These results agree with the actual water table measurements at different piezometers. The GPR estimated water table around Sardon (transect MUSA005) was 1.53 m and the measured water table from the nearby piezometer (psd_0) was 1.51 m and also the GPR estimated water table around mulledes was 2.14 m and the measured water table in Mulledes at Pmu1 well was 2.10 m. Further more, the GPR estimated water table around Trabadilo (*Figure 3.3*) was 1.34 m and the measured water table around this transect was 1.29m.

For the numerical groundwater model the measured water levels were converted into the elevations of the water table (hydraulic heads) for each reference point by subtracting the interpreted depth to the water table from the corresponding DGPS measured elevations of the ground surface.

Table 3: GPR drived water table depths at some selected site

name of transect	X	Y	water_table_depth (m)	hydraulic head (m)
Tbd1	739461.00	4555840.00	2.143	735.09
Tbd2	740717.00	4555330.00	2.756	763.09
Tbd4	739540.00	4556320.00	1.342	733.26
MUSA 001	739404.00	4547860.00	2.143	794.24
MUSA 002	739110.00	4547840.00	2.449	794.84
MUSA 003 1	737620.00	4548700.00	1.837	791.28
MUSA 003 2	737242.00	4548870.00	2.143	797.55
MUSA 004 1	736738.00	4548060.00	2.756	812.94
MUSA 004 2	736830.00	4546980.00	2.143	824.39
MUSA 005	736371.00	4548930.00	1.531	803.06
MUSA 006 1	736542.00	4549040.00	2.449	797.79
MUSA 006 2	736672.00	4549340.00	2.143	786.47
MUSA 006 3	736679.00	4549590.00	2.449	783.83
GJB007 1	737742.00	4551310.00	2.388	749.66
GJB007 2	738103.00	4551280.00	2.449	752.05
GJB007 3	738423.00	4551340.00	2.327	745.72
GJB 0013	736574.00	4551210.00	1.531	762.40
GJB0016	734365.00	4551370.00	2.348	814.39
GB pond	740212.00	4549960.00	2.348	790.97
GJTR	736539.00	4556200.00	2.143	772.42
GJPN2	737027.00	4555760.00	1.837	764.38
3D_TRM008	737268.00	4551730.00	2.327	751.26

3.2. Deriving hydrostatigraphic layers with ERT and VES

3.2.1. ERT

Hard rock aquifers particularly in granitic terrains have extremely different hydraulic parameters than those of porous media as the porosity and permeability are developed due to secondary processes. The secondary porosity introduces much more spatial heterogeneity (Kumar, et al., 2006). So it's difficult to infer the subsurface characteristics based on limited data. In the Sardon catchment the layer thickness was estimated from limited VES points. VES are prone to errors in the interpreted layer resistivity and/or thickness due to limited spatial representation (Dahlin and Loke, 1998). Hence, conducting the ERT could give additional information about the subsurface to fill in the gaps and to constrain the VES interpretations.

The aim of ERT survey was to characterize the stratigraphic units of the catchment. The surveys were conducted at selected representative places so as to have better understanding of the stratigraphic unit at different places. For this, valleys (across and along Sardon River), flat and hilly areas were selected. Besides, for verifications of the ERT performance and inversion, surveys were done in the proximity of existing wells and piezometers. Unfortunately, there was no deep well which could validate the full depth of the resistivity profile. Only shallow wells were used for that purpose.

Most of the ERT results show a three layer stratigraphic unit. The thickness of the first layer ranges from 0.7 to 6m and its resistivity varies from 105 to 5317 ohm-m. The thickness of the second layer ranges from 4 to 35m with a resistivity ranging from 18.5 to 434 ohm-m. Also the resistivity of the third layer ranges from 122 to 4614 ohm-m. However, the thicknesses of these layers vary with in profiles.

Profile mu3 (*Figure 3.6*), was conducted along the main stream at Mulledes just around pmu1 well (*Figure 3.5*). The resistivity log adjacent to that well shows a top layer with a resistivity of 1165 ohm-m and a thickness from 0-0.68m. This top layer is underlain by another layer with a resistivity of 1185 ohm-m and a thickness from 0.68 to 2.11m which again is underlain by a low resistive layer from a thickness of 2.11 to 11.7meter. The higher resistivity layer continues till the bottom of the profile. Correlating with the stratigraphic sequence of the pmu1well the top higher resistivity layers are characterized as soil or unconsolidated rock part and the lower resistivity layer as weathered and fractured granite and the bottom high resistivity layer is considered as massive granite.

Figure 3-5: Photo of Pmu1 well

Profile PN 2 (*Figure 3.7*) which was conducted across the main stream at Penalbo shows a higher resitivity unit on the top part with a thickness of 4m and followed by low resistivity layer with a higher thickness near the stream(just at electrode length 135-165meter). Moreover, in profiles around the high slope areas near Gejo (*Figure 3.8*) and Gejuelo Del Barro (*Figure 3.9*), the weathered granite has a shallow thickness (7-14 meter). This agrees with the work of Tesfai and Attanakaye who claimed that the thickness of the weathered and fractured granite is shallow near less tectonically affected areas and higher around Sardon stream due to the existence of deep structures.

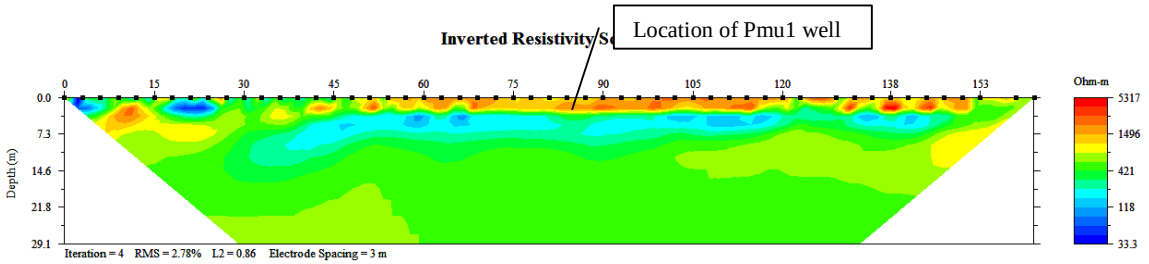

Figure 3-6: Inverted resistivity section of MU3 (profile along Sardon stream around mulledes)

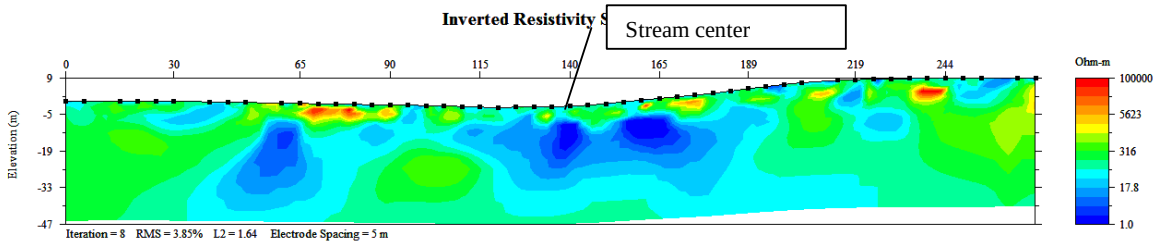

Figure 3-7: inverted resistivity section of profile pn2 (profile across Sardon stream around penalbo)

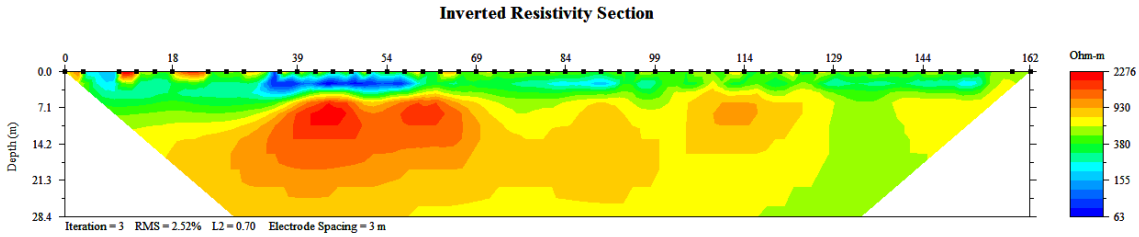

Figure 3-8: inverted resistivity section around GJ_1 well (profiles around Gejo well)

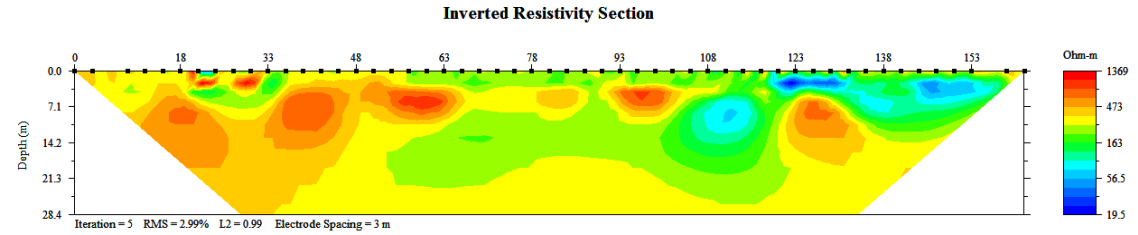

Figure 3-9: inverted resistivity section of GB2 profile (around Gejuelo Del Barro)

3.2.2. VES

Crystalline rocks like granite have no differentiated layers and are not consistent as a body being interpreted on the basis of a layered earth model (Griffiths and King, 1981). The ERT results were used in constraining the re-interpretation of the VES data. In this study 50 Previous VES results with high RMS error and in some cases assuming incorrectly more than three layers, were reinterpreted by constraining to three layer stratigraphic units based on the ERT result. Most of the reinterpreted VES results show a high resistivity top layer underlain by a low resistivity layer which in turn is underlain by a high resistivity layer. These results agree with the ERT results. The reinterpreted resistivity and the thickness values of all the VES results are listed in table (*Table 10, annex*).

3.2.3. Interpolation of hydrostratigraphic layers

For interpolation of the thickness all the re interpreted VES points and selected ERT points were used (*Table 10, annex*). To avoid clustering effect in the interpolation the whole ERT profile was not used for the interpolation only some points were extracted from each profile. Besides, for the interpolation of the top layer the massive and fractured granite outcrops were considered as zero thickness and also for interpolation of the bottom layer the massive granite out crop was considered as zero thickness. The interpolation for both layers was performed using KED (Kriging with External Drift). This interpolation method is proved to be good in condition when the deterministic part of variation (drift) is defined externally as a linear function of some auxiliary variables (Hengl, et al., 2007).

The bottom layer was interpolated using KED with LD (lineament density) as an auxiliary variable. The reason for considering lineament density (*Figure A .2: annex*) as auxiliary variable is due to the fact that the catchment is characterized by lineament or structures. This is evidenced by the ERT and VES results which show that the thickness of the weathered granite is higher around tectonically active areas and lower in less tectonically active areas. The variogram (*Figure 3.14*) model of the bottom layer thickness in relation to LD shows a nugget of 0, a sill of 175 and a range of 2040m. This shows a good relation with bottom layer thickness and LD.

The top layer was interpolated using KED with TPI (topographic position index) as an auxiliary variable since the top layer thickness is higher around the valley (Sardon River) and shallow to none around the sloppy areas. TPI is the difference between a cell elevation value and the average elevation of the neighbourhood around that cell. It is used to categorize the landscape in to valley, hill (high slope) and flat classes (*Figure A1, annex*). The variogram (*Figure 3.15*) model of the top layer thickness in relation to TPI has a nugget of 0.5, sill of 1 and a range of 1725m. This shows a good relation with top layer thickness and TPI.

The interpolated bottom layer (*Figure 3.11*) shows a higher thickness in tectonically active areas and lower thickness in less tectonically active areas. As it can be seen from the profile (*Figure 3.16*), which is extracted from the interpolated bottom layer thickness, around Gejo and Gejuelo Del Barro the bottom layer is thin where as its very thick around the Sardon River this could be due to the prevailing regional fault. Also the interpolated top layer (*Figure 3.13*) has higher thickness near the valley and its thickness decrease in high slope areas. The interpolation results for both of the layers are in good consistency with point resistivity measurement.

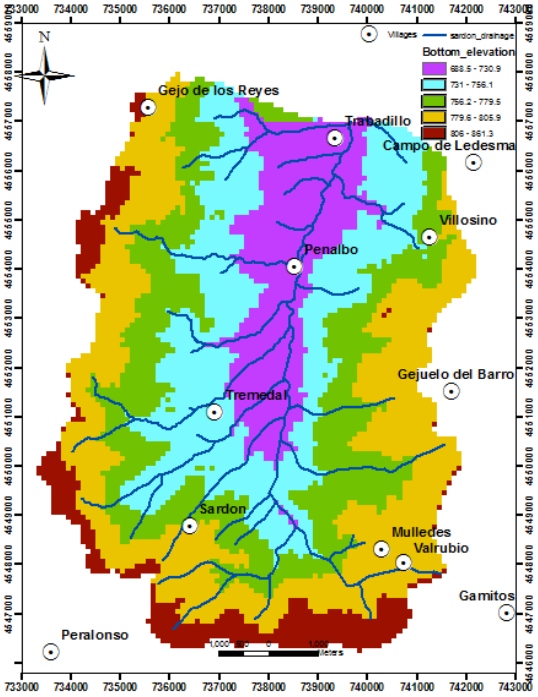

Figure 3-10: Bottom layer Elevation

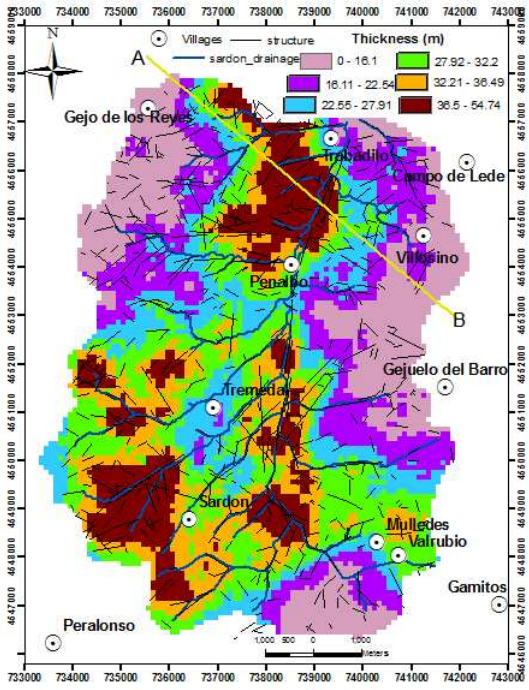

Figure 3-11: Bottom layer Thickness

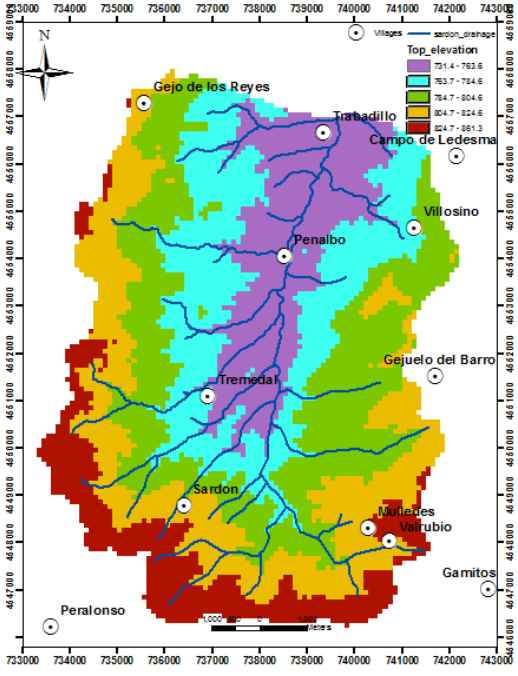

Figure 3-12: Top Layer Elevation

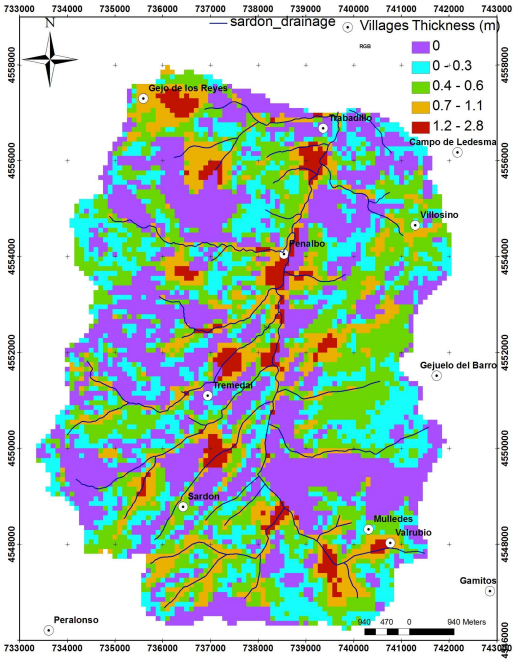

Figure 3-13: Top Layer Thickness

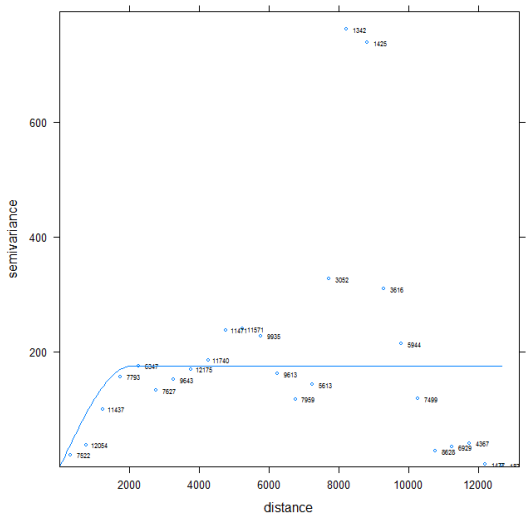

Figure 3-14: Variogram of Bottom layer

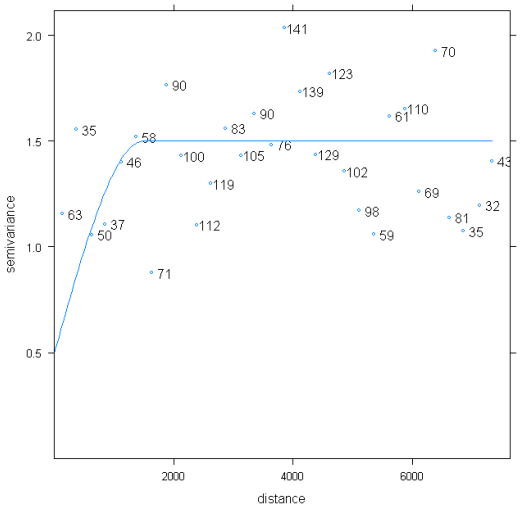

Figure 3-15: Variogram of Top Layer

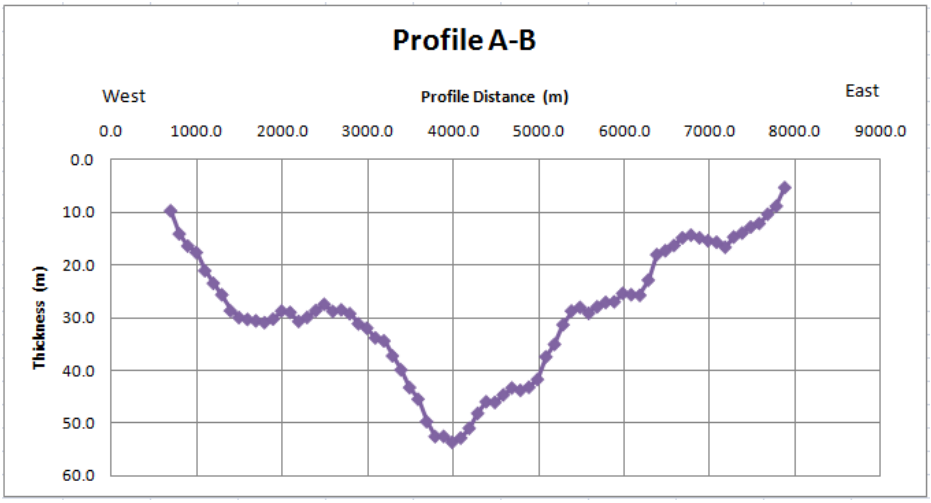

3-16: Profile A-B (For Bottom layer thickness)

3.3. Deriving hydraulic parameters using MRS

3.3.1. Magnetometer

The purpose of the magnetometer survey was to eliminate areas from the MRS surveys on account of earth's field in unfavourable interval values and earth's field variations above acceptable threshold. The field strength of the magnetic field at the earth's surface varies between 60,000 nT near the poles to 30,000 nT at the equator. However, the MRS survey may fail if it is carried out within the field equal to multiple of the power line harmonic frequency which can be defined as follow; 42250-42300, 43425-43475, 44600-44650, 45775-45825 and 46950-47000 (NUMIS manual).

As it is discussed in section 2.5.2 the Magnetic survey was accomplished with two separate magnetometers. The values of the magnetic field measured with the rover were corrected from the diurnal drift measured with the base magnetometer using the Geometrics software (MagMap2000). By removing the temporal variation from the rover, only the residual magnetic field remains. Hence, the earth magnetic field after the diurnal correction was 44794nT. This was fortunately out of the unfavorable earth's magnetic field interval so the survey could be carried out.

The rover magnetometer readings were taken as a transect or in a 6 by 6 gridded profile with 20m interval between each other. To identify variation of earth magnetic field with in the readings their average, standard deviation and the difference between the maximum and minimum were calculated. As it can be seen from (*Table 4*) for most of the measurements the difference between the maximum and the minimum readings ranges between 10.2 and 3.1 which is below the threshold (<50nt) and also the standard deviation ranges from 0.9 to 2.4 which is again below the maximum threshold (<20nt stde). Hence, all the results show that there is no existing magnetic anomaly in the area that could affect the magnetic resonance survey.

Table 4: Magnetometer survey result (all values are in nano Tesla (nt))

SITE	no.p	Std.Dev.	Min.	1stQu.	Median	Mean	3rdQu.	Max.	MaxMin	Var.
Muelledes transect	63	2.4	44791.0	44793.2	44795.4	44795.4	44797.2	44800.7	9.7	5.7
Psd2	27	1.0	44791.9	44792.9	44793.4	44793.7	44794.6	44795.7	3.8	1.1
SardonEst	6	1.1	44794.6	44796.4	44796.6	44796.5	44797.2	44797.7	3.1	1.2
PradosFuentes	10	1.8	44797.0	44797.8	44799.7	44799.3	44800.2	44802.2	5.2	3.1
TremedalE	6	1.7	44801.1	44801.3	44802.1	44802.6	44804.0	44805.0	3.9	2.9
TremedalPcl7	26	0.9	44802.0	44803.0	44803.4	44803.6	44804.3	44805.1	3.1	0.9
Pcl5	24	1.8	44804.1	44805.6	44806.9	44807.1	44808.9	44809.7	5.6	3.3
PenalboS	68	1.9	44803.5	44805.9	44807.1	44807.3	44808.3	44813.7	10.2	3.7
Gejuelo	36	1.2	44804.5	44805.9	44806.7	44806.8	44807.8	44809.1	4.6	1.4
PenalboEst	36	1.3	44804.9	44807.5	44808.3	44808.4	44809.4	44810.9	6.0	1.7
Muelledes grid	36	1.5	44790.4	44792.4	44793.3	44793.2	44794.3	44795.7	5.3	2.1
TremedalGejuelo	36	1.5	44803.3	44804.6	44805.4	44805.8	44807.0	44809.1	5.8	2.3
PenalboWest	36	1.5	44807.5	44809.4	44810.8	44810.5	44811.8	44813.3	5.8	2.3
PenalboWW	36	1.6	44802.9	44804.4	44805.2	44805.4	44806.1	44810.6	7.7	2.5
Gejo	36	1.7	44817.2	44818.6	44819.2	44819.6	44820.3	44824.0	6.8	2.7
TremedalSWOleario	36	1.7	44796.5	44797.8	44798.8	44799.1	44800.1	44802.6	6.1	2.8
GejoPenalbo	36	1.8	44810.2	44811.8	44812.4	44813.0	44813.8	44817.0	6.8	3.4
Trabadillo	36	1.9	44811.9	44813.1	44814.1	44814.6	44816.3	44818.7	6.8	3.6
PenalboSouth	36	1.9	44800.7	44805.3	44806.3	44806.5	44807.4	44810.1	9.4	3.8
Total	629	7.4	44790.4	44799.2	44806.1	44805.2	44809.4	44824.0	33.6	54.8

Max value

3.3.2. MRS

Even though magnetometer survey conducted as a pre-survey indicated favourable earth magnetic field, in most of the MRS surveys signal was not detected and in some sites signal was very weak due to very low subsurface water storage. In the survey a square loop size of 15, 30, 60 and 80 was applied. Only the MRS survey (*Figure 3.17*), which was conducted at Sardon stream near Tremedal Village indicated significant MRS signal. It showed zero water content and low decay time constant at the top part with a thickness of 2m underlain by a layer with a water content of 4.6 %, and decay time constant of 0.3 second and a thickness of 14m underlain by a layer with a higher water content and higher decay time constant (*Table 5*) directly correlated with hydraulic conductivity.

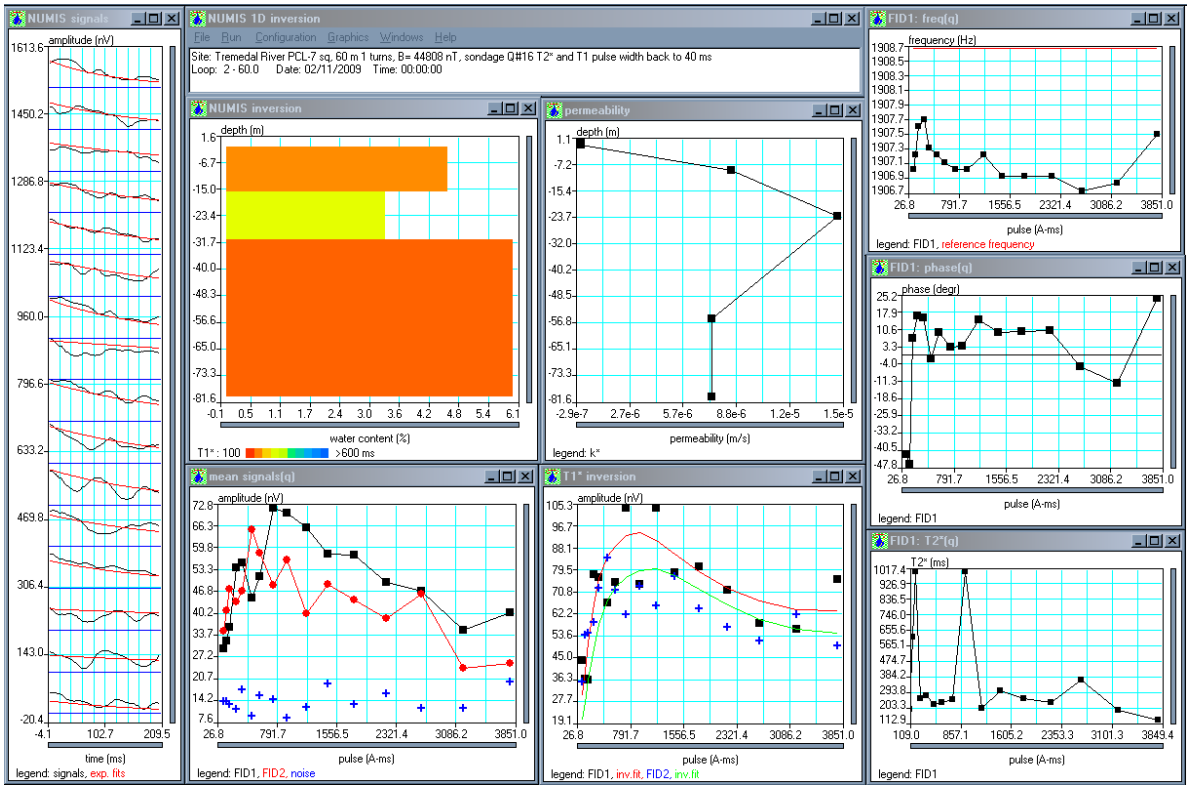

Figure 3-17: MRS result (around Sardon Stream)

Table 5:MRS result

Top (m)	Bottom (m)	Free water content (%)	T2* (s)	T1* (s)
0.5	2	0.0%	0.010	0.050
2	16	4.6%	0.310	0.162
16	31	3.3%	0.400	0.250
31	80	6.0%	0.066	0.133

Curve fitting assessment (RMS, nV)

FID	RMS (nV)
1	9.8
2	7.7

As analysed by Francis (2010) the MRS inversion result shows hydraulic conductivity for the top layer which ranges from 1.5 to $3x10^{-5}$ m/s (1.296 to 2.6 m/day) and for the bottom layer from 1.5 to $3x\ 10^{-7}$ m/s (0.01296 to 0.026 m/day). This lower value for the top layer could be related to the existence of more clayey materials around the Sardon fault zone at which the survey was conducted. Nevertheless, these results strengthen the idea of existence of thick aquifer (weathered-fractured granite) at the Sardon fault zone aligned also with main catchment Sardon River.

3.4. Steady state flow model

The steady state model of the Sardon catchment was developed by Lubczynski and Gurwin (2005). The model has 100 m cell size, covering the total area of Sardon catchment. The extent of the model is 80 km2 with 10 km length and 8 km width. The numerical model comprised two layered structure. The thickness of these layers was obtained from interpolation of 59 VES data (Tesfai, 2000) in conjunction with 90m SRTM DEM. In this study these layers were modified using points combined with 5m resolution DEM obtained from Spanish Geological Survey. The details of the interpolation of the new set of layers are discussed in section 3.2.2.

3.4.1. Hydraulic heads

In the previous steady state model, 23 field measured hydraulic head values and 14 fictitious groundwater levels derived by regression method were used for the interpolation of point heads to obtain initial head distributed map and for the final steady state calibration. In this study besides the 23 existing piezometers 22 GPR estimated water table depths were used for the interpolation of point heads to obtain initial hydraulic head. Further more, these values were used for the final steady state model calibration. The fictitious data that were used in the previous are not included in the current model. They are replaced by the 22 GPR estimated water table depths.

3.4.2. Boundary conditions

There was no change in the location of boundary condition cells as compared to former model (Lubczynski and Gurwin, 2005). This means, no flow boundary conditions have been assigned along the all external boundaries of the catchment, considering the topography, geology and structure of the area which indicated well defined water divides. Sardon River, which flows along the major fault zone, was simulated by drain boundary condition in which the drain elevation was selected as bottom of the river while the drain boundary conductance was slightly optimized.

3.4.3. Groundwater fluxes

Groundwater fluxes comprise: recharge (R), groundwater evapotranspiration (ETg) and groundwater outflow (Qout).

Recharge

Recharge in the study area depends entirely on the precipitation of the area and it varies from place to place due to heterogeneity of the medium. In this model, the recharge was calculated by chloride mass balance method (CMB) method so it represents the long term average recharge well reflecting steady-state model conditions.

Groundwater evapotranspiration (ETg)

The ETg occurs either as Eg when the water level is close to the land surface or as Tg through phreatophytes characterized by deep roots tapping groundwater. The ETg was simulated in the model by evapotranspiration package of MODFLOW and the different zones were defined based on the results of the SEBAL solution, explained in chapter. The elevation of the ET surface in the MODFLOW was assumed as the topographical surface and the extinction depth was set 5.0 m considering the maximum rooting depth of the area.

Groundwater outflow

The groundwater outflow from the aquifer in the model was simulated by drain package representing main Sardon river course matching regional fault system zone. Groundwater flow occurs when aquifer hydraulic head is greater than the defined drain elevation and ceases when aquifer hydraulic head falls below the defined drain elevation. The groundwater outflow to the drain (Q_d) was calculated by;

$$Q_d = C_d.(h - d) \qquad (11)$$

Where $C_d = KL$ and K is equivalent hydraulic conductivity, L is length of the drain within a cell, h aquifer hydraulic head and d elevation of the drain. The value of C_d was adjusted during the calibration process.

Hydraulic conductivity

The hydraulic conductivity varied spatially and the zones were defined in the first layer based on the geophysical analysis, slug tests and borehole investigations with soil sample analysis performed in the previous fieldworks. These zoned maps prepared in ILWIS were imported into MODFLOW as an ASCI file and finally adjusted during steady state model calibration (Lubczynski and Gurwin, 2005). The second weathered fractured granite layer was zoned using GIS cross overlay procedure. The MRS derived hydraulic conductivity was used in constraining the optimization of hydraulic conductivity of the zones.

3.4.4. Model calibration

The model calibration is achieved by optimizing the set of parameters and conditions in the simulated model which reproduce the calibration target, i.e. field observed values (Anderson and Woessner, 1992). The calibration of the steady state flow model of Sardon was carried out using both trial and error method and Pest. The model was recalibrated using a total of 45 hydraulic head data at different locations; drain conductance data obtained by slug tests, recharge values obtained from chloride mass balance method which represented long term flux and other information for better optimization. The hydraulic conductivity zones defined in the previous model calibration by Lubczynski and Gurwin (2005) were altered by the MRS derived hydraulic conductivity results.

The steady state model was calibrated initially by readjusting the hydraulic conductivity with manual trial and error method and later by automated parameters estimation programme, PEST (Doherty, 2000). However, calibration with PEST was not successful due to the drying of some observation wells during the iteration process that caused the programme to stop before the solution was converged. Hence, the calibration was finally performed manually using trial and error method.

3.4.5. Head calibration target

The model calibration error can be analysed qualitatively by mean error (ME), mean absolute error (MAE) and root mean square error (RMSE). The mean error is the mean differences between simulated hydraulic head (hc) and observed hydraulic head (ho):

$$ME = \frac{1}{n}\sum_{i=1}^{n}(h_c - h_o)_i \qquad (12)$$

The mean absolute error (MAE) is the mean of the absolute value of the differences in simulated hydraulic head (h_c) and observed hydraulic head (h_o):

$$MAE = \frac{1}{n}\sum_{i=1}^{n}|(h_c - h_o)_i| \qquad (13)$$

The root mean squared error (RMSE) is the average of the squared differences in simulated hydraulic head (h_c) and observed hydraulic head (h_o):

$$RMSE = \left[\frac{1}{n} \sum_{i=1}^{n} (h_c - h_o)_i^2 \right]^{0.5} \quad (14)$$

Where n is the number of observations.

Based on the above mentioned error analysis equations, the error of the calibration carried out over the 22 GPR estimated hydraulic heads and 23 piezometers is presented in Table 6. During calibration Gejo well was sensitive for hydraulic conductivity changes. It mostly went dry for slight change in hydraulic conductivity. This could be due to its thin aquifer thickness as it is evidenced by the ERT result.

Table 6: Calibration error analysis

ME	0.428 m
MAE	14.36 m
RMSE	10.01 m

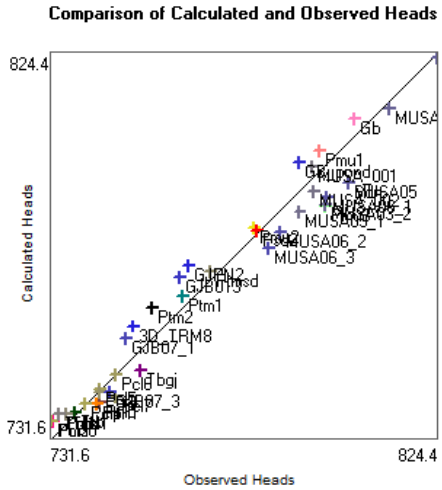

Figure 3-18: Scatter plot of steady state simulated vs. observed hydraulic heads

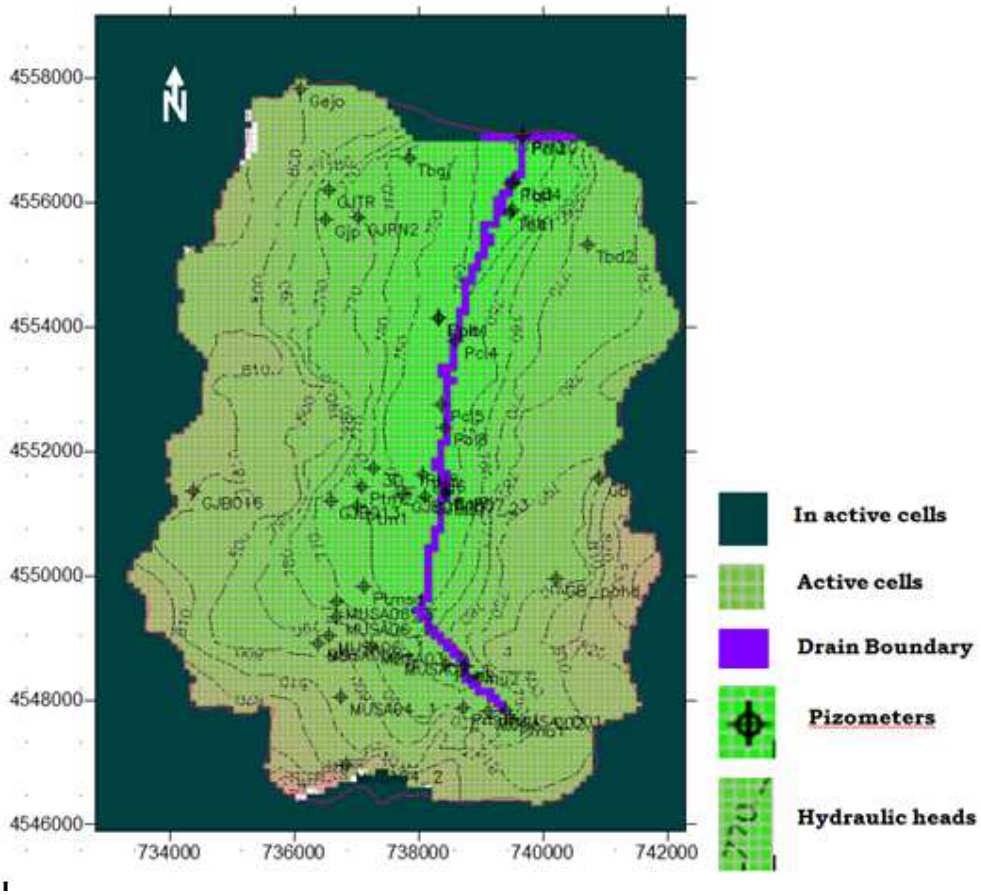

Figure 3-19: Steady state hydraulic head distribution in the calibrated model

3.4.6. Hydraulic conductivity

In the calibration process, the hydraulic conductivity values used in the previous model of Lubczynski and Gurwin (2005) were adjusted based on the MRS derived hydraulic conductivities, new hydrostratigraphy and new adjusted fluxes. The hydraulic conductivity in upper layer showed higher values compared to lower weathered fractured granite layer although the lower layer has larger thickness so because of that also larger trasnmissivity. The hydraulic conductivity varied from 0.8 to 19 m/day in first layer with highest conductivity along the Sardon river course towards the upper catchment. In the second layer, hydraulic conductivity varied from 0.05 to 1.5 m/day and the hydraulic conductivity zones were clustered into smaller areas compared to the first layer, possibly due to local fracture networks.

3.4.7. Water budget

The water budget components in the calibrated model domain show the influx and outflux of groundwater within the aquifer system. The only source of influx to the model is recharge from precipitation. While the outflux from the system is ET_g and river discharge at catchment outlet. The overall water budget of the model could be formulated as following equation.

$$R_{pptn} = ET_g + G_{of} \pm \Delta S \qquad (15)$$

Where R_{pptn}, ET_g, G_{of} and ΔS are the recharge from precipitation, groundwater evapotranspiration, groundwater outflow to the drain and change in the groundwater storage, which is equal to zero for the case of steady state, respectively.

Table 7: Steady state water balance of the model (all figures are in m^3/day)

```
 ============================================================
 WATER BUDGET OF THE WHOLE MODEL DOMAIN:
 ============================================================

        FLOW TERM              IN              OUT          IN-OUT
          STORAGE  0.0000000E+00  0.0000000E+00  0.0000000E+00
    CONSTANT HEAD  0.0000000E+00  0.0000000E+00  0.0000000E+00
            WELLS  0.0000000E+00  0.0000000E+00  0.0000000E+00
           DRAINS  0.0000000E+00  1.2674748E+04 -1.2674748E+04
         RECHARGE  1.3170601E+04  0.0000000E+00  1.3170601E+04
               ET  0.0000000E+00  4.9534027E+02 -4.9534027E+02
    RIVER LEAKAGE  0.0000000E+00  0.0000000E+00  0.0000000E+00
  HEAD DEP BOUNDS  0.0000000E+00  0.0000000E+00  0.0000000E+00
   STREAM LEAKAGE  0.0000000E+00  0.0000000E+00  0.0000000E+00
 INTERBED STORAGE  0.0000000E+00  0.0000000E+00  0.0000000E+00
 MULTI-AQIFR WELL  0.0000000E+00  0.0000000E+00  0.0000000E+00
------------------------------------------------------------
              SUM  1.3170601E+04  1.3170088E+04  5.1269531E-01
  DISCREPANCY [%]  0.00
```

The long term average of fluxes is represented in the water balance calculated by the steady state model. The recharge(R) is 13170 m^3/day (60.1mm/y, ET_g is 495.3 m^3/day (2.26mm/y) and groundwater outflow (G_{of}) is 12674 m^3/day (57.8mm/y). Illustrative diagram of water balance of the calibrated steady state model is shown in Figure 3.20

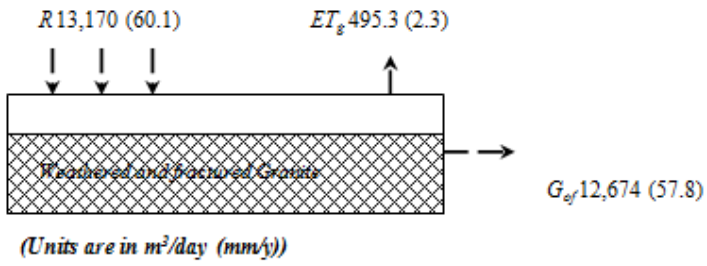

Figure 3-20: water budget components of the calibrated model

Table 8: The water balance of the previous model and recalibrated steady state model

	Previous model(2005)	Ruwan (2009)	Recalibrated model
Recharge	56.0	70.7	60.1
ET_g	20.0	22.0	2.3
G_{of}	36.0	48.7	57.8

As shown in table 8, the results of recalibrated model are comparable with the previous model in case of recharge and groundwater outflow but the evapotranspiration is very low in this model.

4. Conclusion and recommendation

The main objective of the research was to improve groundwater flow model of Sardon catchment by determining additional model input data using hydro geophysics. This was achieved by; constraining the model by using additional GPR estimated water table depths, by modifying the model geometry using ERT and VES characterized hydrostratigraphic layers and by modifying the model hydraulic parameters using MRS derived hydraulic conductivity. The largest improvement as compared to the previous model that was used as starting point of this work is that this model is constrained by additional 22 GPR estimated hydraulic heads. The model geometry is modified with layers interpolated from 80 ERT and VES points and the hydraulic parameter was modified based on the newly derived MRS hydraulic conductivity.

GPR estimated water table depths ranges from 1.342 to 2.756 meter over the investigated points. The maximum depth was obtained around the north eastern part of the catchment and the minimum around the Sardon River. These results well agree with the actual water table measurements at different piezometers. The results of this study indicate that ground penetrating radar (GPR) techniques may be employed in some areas to quickly, cheaply and accurately estimate elevations of shallow groundwater tables.

During the GPR interpretation the conversion of two ways arrival time into depth was performed manually using mathematical equations. Due to this time consuming manual calculations, the conversion was performed to selected GPR Profiles. Hence a further conversion is recommended on the remaining profiles which might serve as additional constrain of the flow model. In line with this, it will be better if automatic conversion codes are developed for fast and efficient conversion.

Based on the ERT and previous VES results the hydrostratigaphic layers of the Sardon catchment were characterized as a top high resistivity unconsolidated soil layer underlain by a low resistivity weathered and fractured granite which in turn was underlain by a high resistivity massive granite. The thicknesses of the three layers showed large spatial variability. The thickness of the weathered and fractured granite was highest around the Sardon stream due to the prevailing regional Sardon fault. The MRS also confirms the occurrence of high thickness aquifer around the Sardon stream.

The modified steady state model gives a recharge(R) of 13170 m^3/day (60.1mm/y, ET_g of 495.3 m^3/day (2.26mm/y) and groundwater outflow (G_{of}) of 12674 m^3/day (57.8mm/y). The recharge and groundwater outflow results are comparable with the previous model but the ET_g is lower in this model. This lower value could be due to the fact that the model was not better calibrated due to time constraint. How ever, if the model was better calibrated these results could be different.

The calibration of the steady state model using PEST optimization was not successful since PEST stops before convergence due to existence of dry well. Hence, a better link between PEST and MODFLOW is needed for fast and efficient calibration.

Reference

A. Giocoli, P. Burrato, P. Galli, V. Lapenna, S. Piscitelli, E. Rizzo, G. Romano, A. Siniscalchi, C. Magr`ı a, Vannoli P (2008) Using the ERT method in tectonically active areas: hints from Southern Apennine (Italy). Advances in Geosciences

Anderson MP, Woessner WW (1992) Applied groundwater modeling : simulation of flow and advective transport Academic Press, San Diego etc.

Annan AP (2002) GPR—History, Trends, and Future Developments. Subsurface Sensing Technologies and Applications 3: 253-270

Annan AP (2005) GPR Methods for Hydrogeological Studies:185-213.

Attanayake NB (1999) Analysis of fractures in a granitic terrain and their tectonic and hydrogeological implications : a study from Sardon catchment area, Salamanca province, Spain. M.Sc ITC

Baker R, Moore J (1998) The application of time-lapse electrical tomography in groundwater studies. The Leading Edge 17: 1454-1458

Boucher M, Favreau G, Vouillamoz J, Nazoumou Y, Legchenko A (2009) Estimating specific yield and transmissivity with magnetic resonance sounding in an unconfined sandstone aquifer (Niger). Hydrogeology Journal

Caputo R, Piscitelli S, Oliveto A, Rizzo E, Lapenna V (2003) The use of electrical resistivity tomographies in active tectonics: examples from the Tyrnavos Basin, Greece. Journal of Geodynamics 36: 19-35

Colella A, Lapenna V, Rizzo E (2004) High-resolution imaging of the High Agri Valley Basin (Southern Italy) with electrical resistivity tomography. Tectonophysics 386: 29-40

Cornejo U, S.P (2000) Groundwater recharge modelling in hard rocks area : Sardon case study, Spain. MSc, ITC

Dahlin T, Loke MH (1998) Resolution of 2D Wenner resistivity imaging as assessed by numerical modelling. Journal of Applied Geophysics 38: 237-249

Daily W, Ramirez A, Binley A, LeBrecque D (2004) Electrical resistance tomography. The Leading Edge 23: 438-442 DOI 10.1190/1.1729225

Daniels DJ (2004) Ground Penetrating radar, second edn,IET(the institute of Engineering and technology)

Davis JL, Annan AP (1989) GROUND-PENETRATING RADAR FOR HIGH-RESOLUTION MAPPING OF SOIL AND ROCK STRATIGRAPHY. Geophys Prospect 37: 531-551

Doherty J (2000) PEST-Model-Independant Parameter Estimation, User's Manual. Water Mark Computing

Doolittle JA, Jenkinson B, Hopkins D, Ulmer M, Tuttle W (2006) Hydropedological investigations with ground-penetrating radar (GPR): Estimating water-table depths and local ground-water flow pattern in areas of coarse-textured soils, pp. 317-329.

Duah A (1999) Groundwater recharge modeling in hard rocks using remote sensing and GIS applications : a case study in the rio Tormes basin Salamanca province, Spain. MSc, ITC

Freeze RA, Cherry JA (1979.) Groundwater Prentice-Hall, Inc, Englewood Cliffs, NJ.

Goldman M, Rabinovich B, Rabinovich M, Gilad D, Gev I, Schirov M (1994) Application of the integrated NMR-TDEM method in groundwater exploration in Israel. Journal of Applied Geophysics 31: 27-52

Griffiths DH, Barker RD (1993) Two-dimensional resistivity imaging and modelling in areas of complex geology. Journal of Applied Geophysics 29: 211-226

Griffiths DH, King RF (1981) Applied geophysics for geologists and engineers : the elements of geophysical prospecting, Second edition edn Pergamon Press, Oxford etc.

Hengl T, Heuvelink GBM, Rossiter DG (2007) About regression-kriging: From equations to case studies. Computers & Geosciences 33: 1301-1315

Hubbard SS, Rubin Y (2000) Hydrogeological parameter estimation using geophysical data: a review of selected techniques. Journal of Contaminant Hydrology 45: 3-34

Iivari TA, Doolittle JA (1994) Computer simulations of depths to water table using ground-penetrating radar in topographically diverse terrains. In: Kovar, K, Soveri, J (Eds), Ground Water Quality Management Proceedings of GQM 93, International Association of Hydrological Sciences, Tallinn, Estonia, September 1993, : pp. 11- 20.

Kemna A, Kulessa B, Vereecken H (2002) Imaging and Characterization of Subsurface Solute Transport using Electrical Resitivity Tomography (ERT) and Equivalent Transport Model. Journal of hydrology 267: 125-146 DOI 10.1016/S0022-1694(02)00145-2

Kirsch Re (2006) Groundwater geophysics : a tool for hydrogeology Springer, Berlin.

kumar D, S. Ahmed, N.S.Krishnamurthy, B.t Dewandel (2006) Reducing ambiguities in vertical electrical sounding interpreations; A geostastistical application. journal of Applied Geophysics

Legchenko A, Baltassat J-M, Bobachev A, Martin C, Robain H, Vouillamoz J-M (2004) Magnetic Resonance Sounding Applied to Aquifer Characterization. GROUND WATER 42: 363-373

Lopez P, Carnicero A (1987) Hercynian plutonism of the Salamanca-Zamora peneplain (Central western Spain). In Geologia de los granitoids y rocas asociadas del macizo

Lubczynski M, Gurwin J (2005) Integration of various data sources for transient groundwater modeling with spatio-temporally variable fluxes--Sardon study case, Spain. Journal of hydrology 306: 71-96

Lubczynski M, Roy J (2007) Use of MRS for hydrogeological system parameterization and modeling. Boletin Geologico y Minero 118 (2007): 509–530

Mastrocicco M, Vignoli G, Colombani N, Zeid N (2009) Surface electrical resistivity tomography and hydrogeological characterization to constrain groundwater flow modeling in an agricultural field site near Ferrara (Italy). Environmental Earth Sciences

Nakashima Y, Zhou H, Sato M (2001) Estimation of groundwater level by GPR in an area with multiple ambiguous reflections. Journal of Applied Geophysics 47: 241-249

Richardson JL, Wilding LP, Daniels RB (1992) Recharge and discharge of groundwater in aquic conditions illustrated with flownet analysis. Geoderma 53: 65-78

Roy J, Lubczynski M (2003) The magnetic resonance sounding technique and its use for groundwater investigations. Hydrogeology Journal 11: 455-465 DOI 10.1007/s10040-003-0254-8

Ruwan GR (2009) Numerical groundwater flow and solute transport modelling : a case study of Sardon catchment in Spain. MSc. Thesis, ITC

Seaton WJ, Burbey TJ (2002) Evaluation of two-dimensional resistivity methods in a fractured crystalline-rock terrane. Journal of Applied Geophysics 51: 21-41

Sellmann PV, Arcone SA, Delaney AJ (1983.) Radar profiling of buried reflectors and the ground water table. USA Cold Region Research and Engineering Laboratory Report 83-11Hanover, New Hampshire

Shakya DR (2001) Spatial and temporal groundwater modeling integrated with remote sensing and GIS : hard rock experimental catchment, Sardon, Spain. MSc, ITC

Smith MC, Vellidis G, Thomas DL, Breve MA (1992) Measurement of Water Table Fluctutuations in a sandy soil using Ground Penetrating Radar,. Trans ASAE 35,: 1161-1166,

Tesfai BH (2000) Subsurface characterization of granitic basement from structural and resistivity data : a case study from Sardon catchment area, Salamanca, Spain. MSc, ITC

Annex A: maps

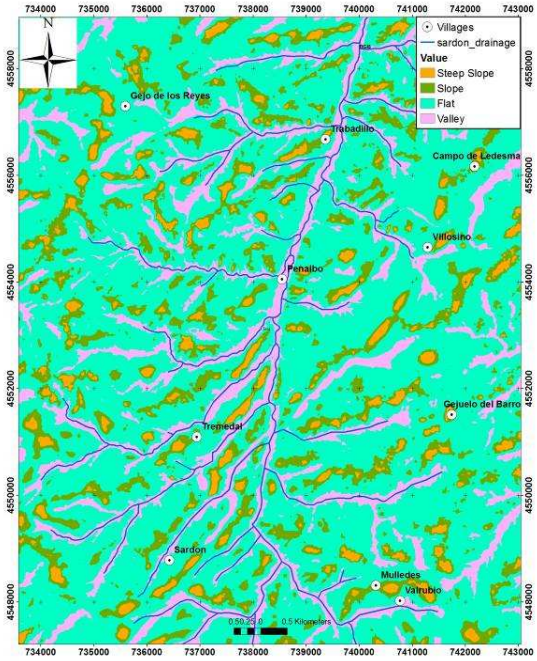

Figure A 1: map of TPI (Topographic Position Index)

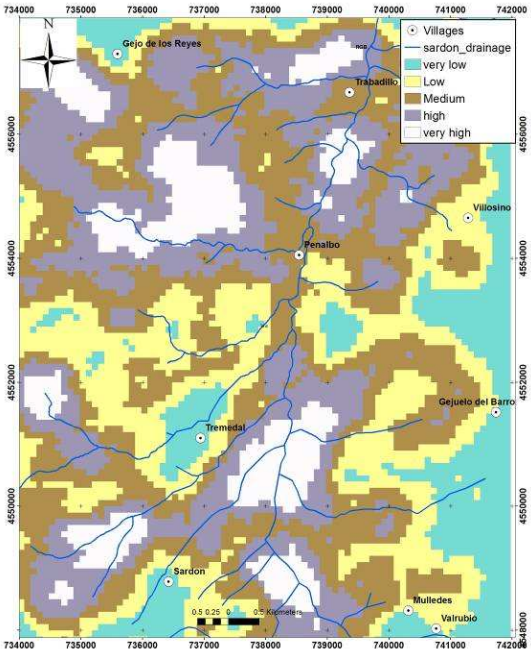

Figure A 2:lineament density

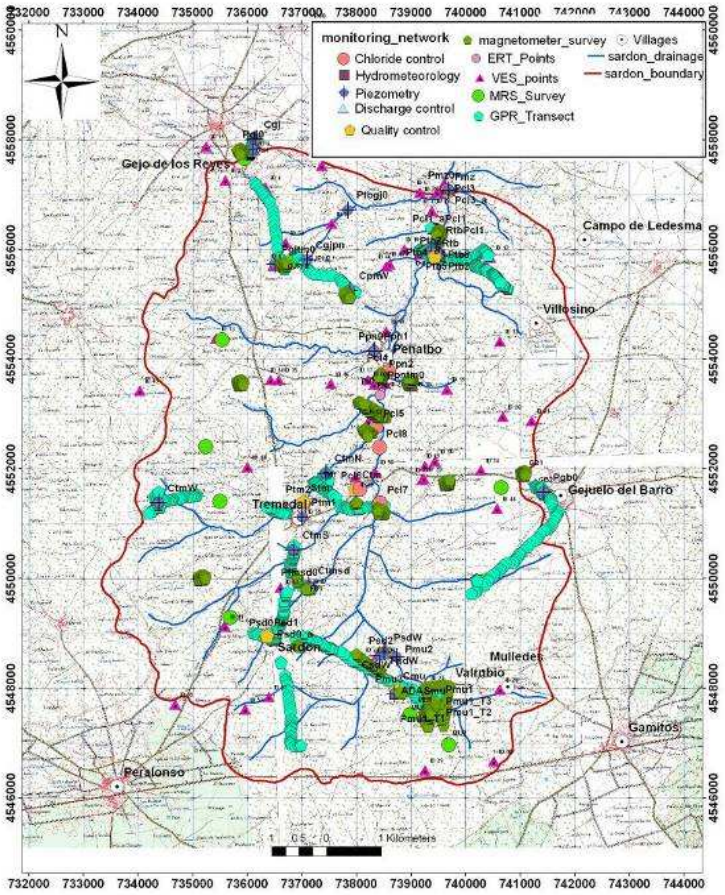

Figure A 3: All Hydro-geophysical survey Sites

Annex B: Selected GPR profiles

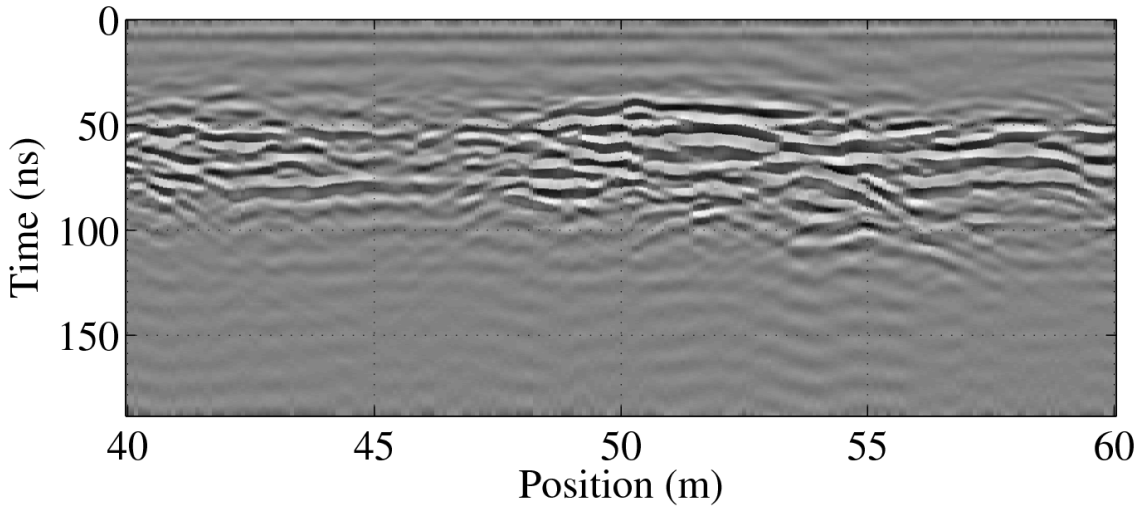

Figure B 1: Profile TBD1

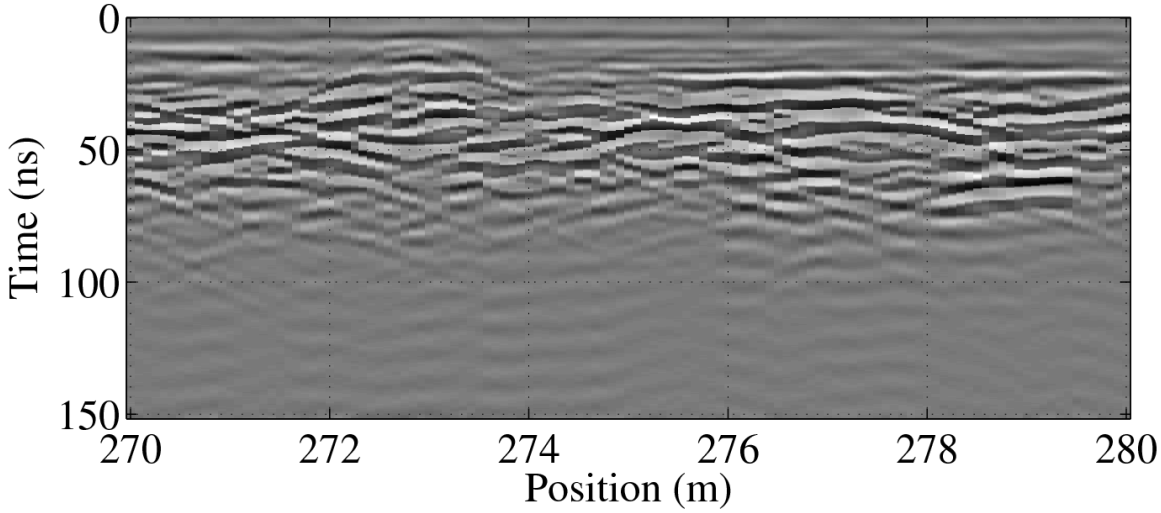

Figure B 2: Profile Musa005

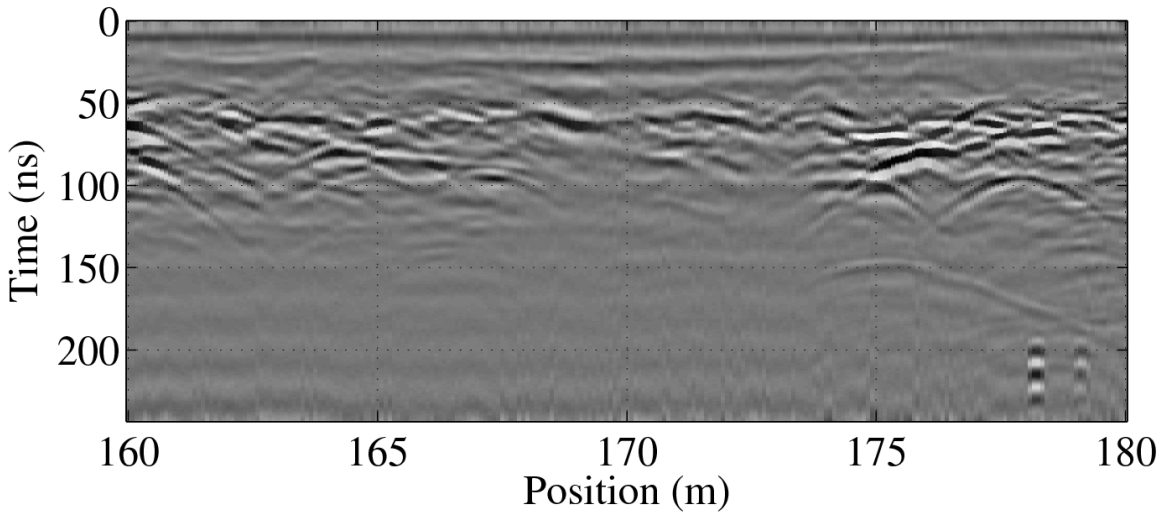

Figure B 3: Profile Musa006_1

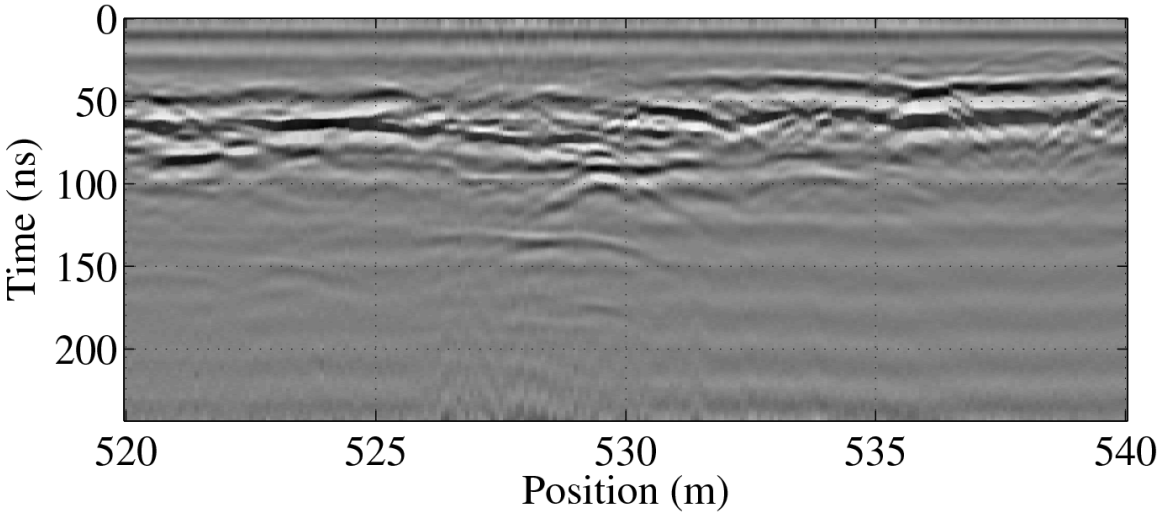

Figure B 4: Profile Musa006_2

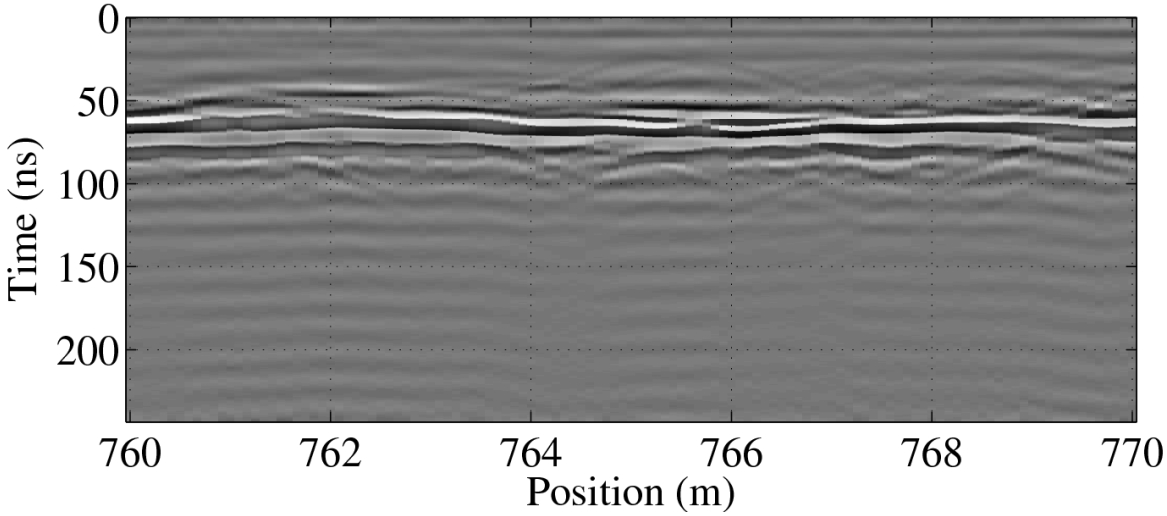

Figure B 5:Profile Musa006_3

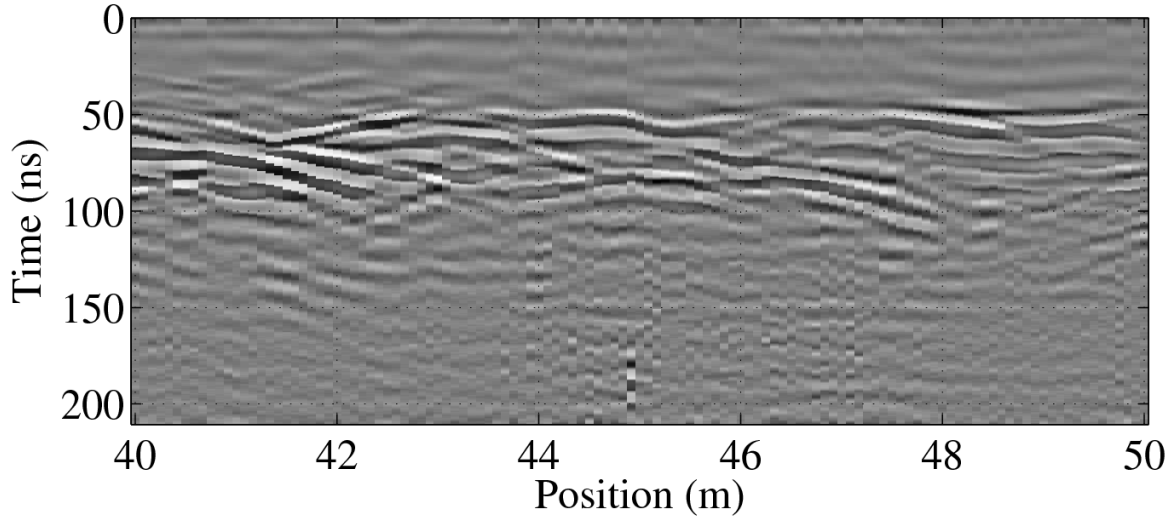

Figure B 6: Profile GJB007_1

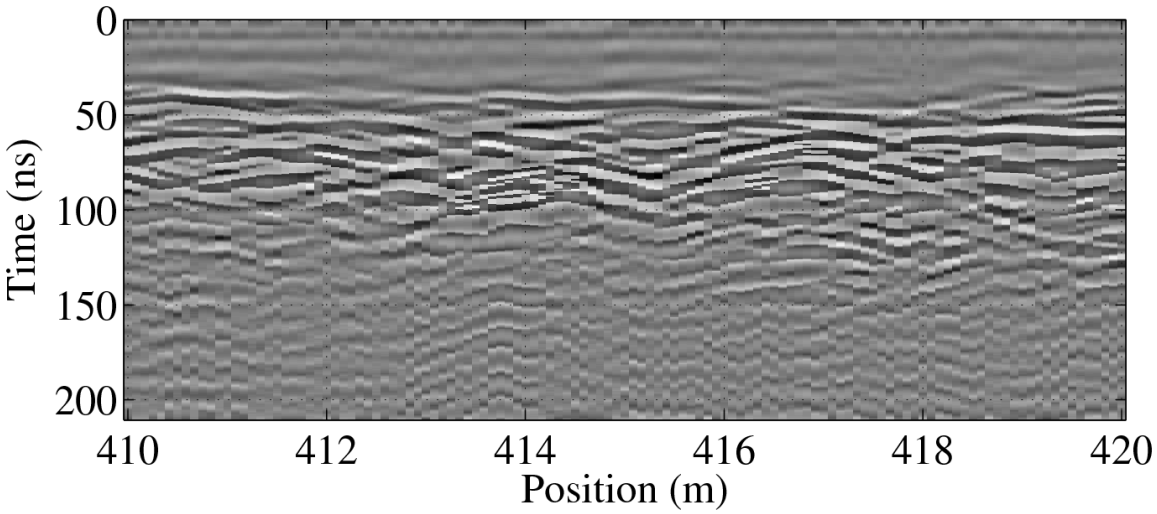

Figure B 7: Profile GJB007_2

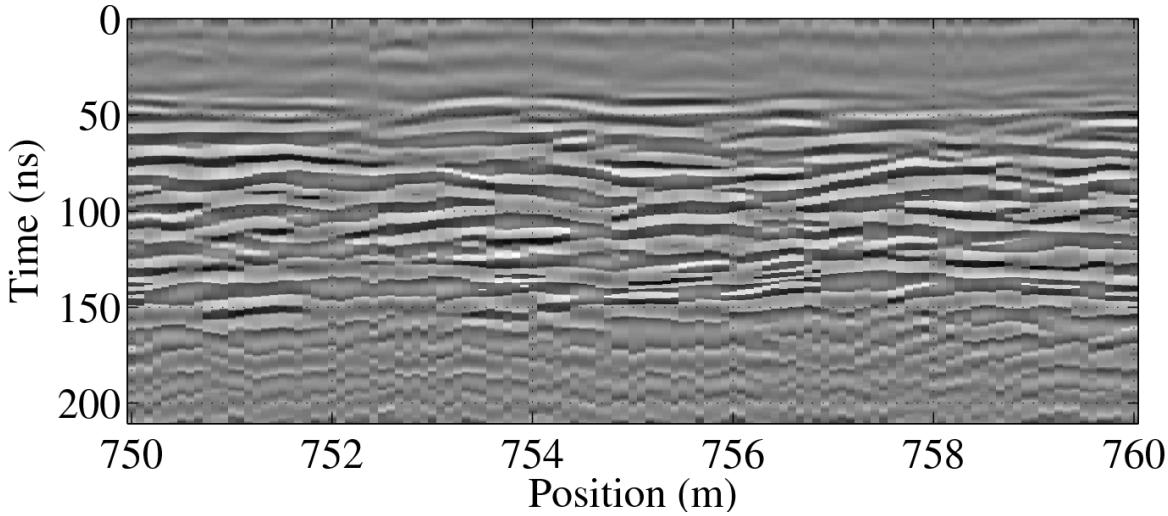

Figure B 8: Profile GJB007_3

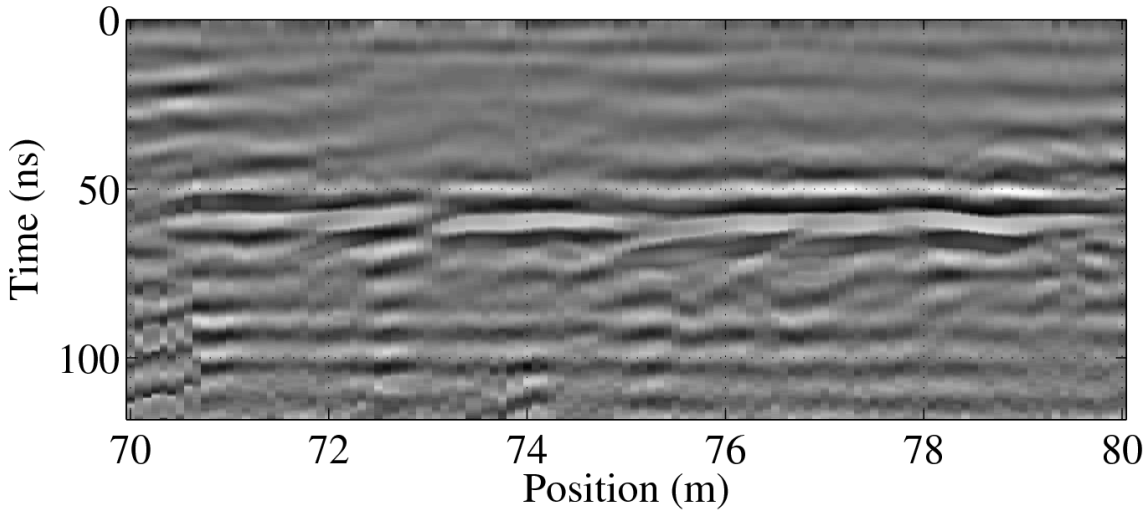

Figure B 9: Profile Tbd2

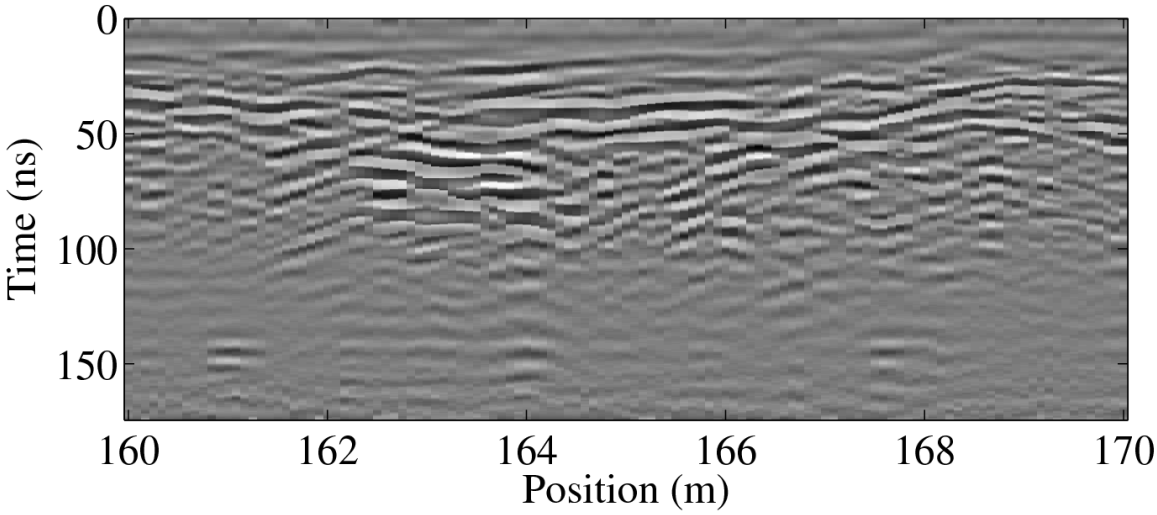

Figure B 10: Profile GJB0013

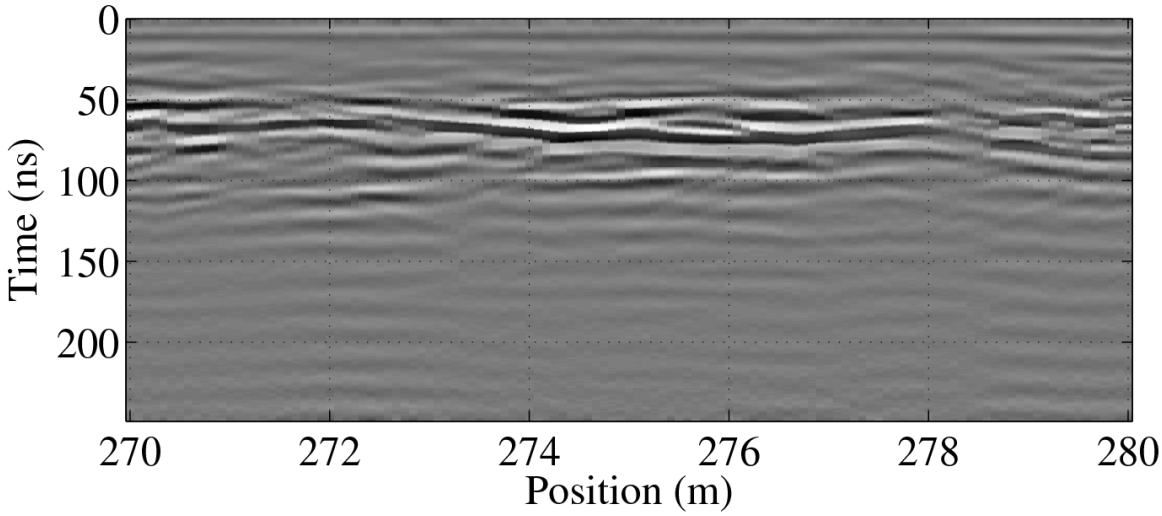

Figure B 11: Profile GJB0015

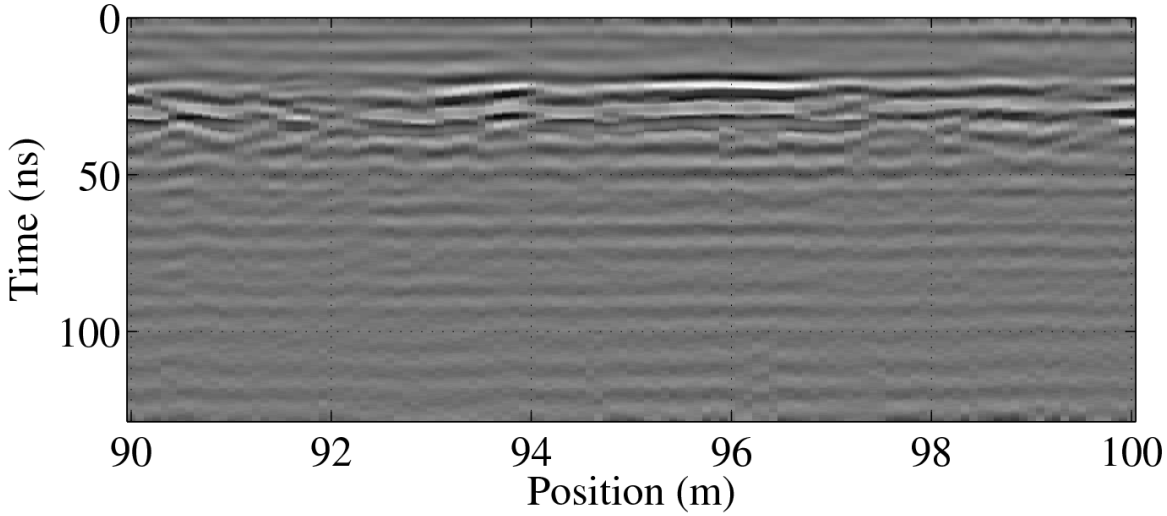

Figure B 12: Profile GJB0016

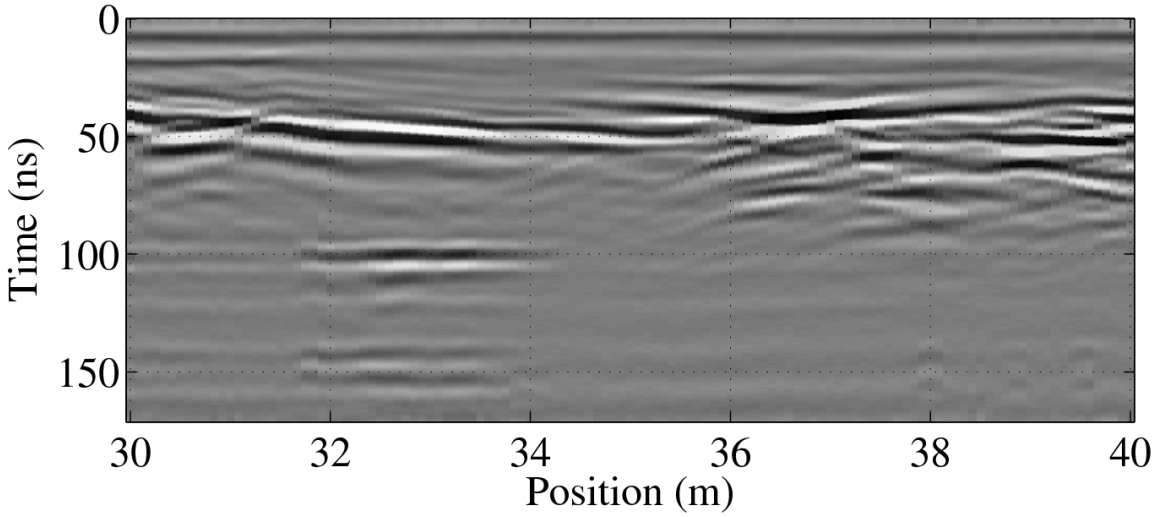

Figure B 13: Profile 3D TRM 008

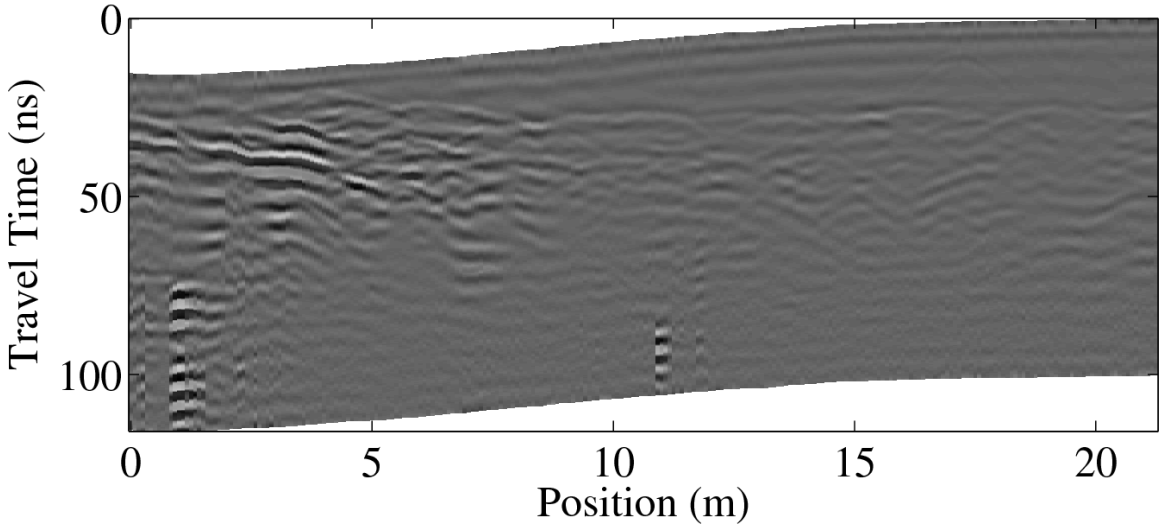

Figure B 14: Profile GJB pond

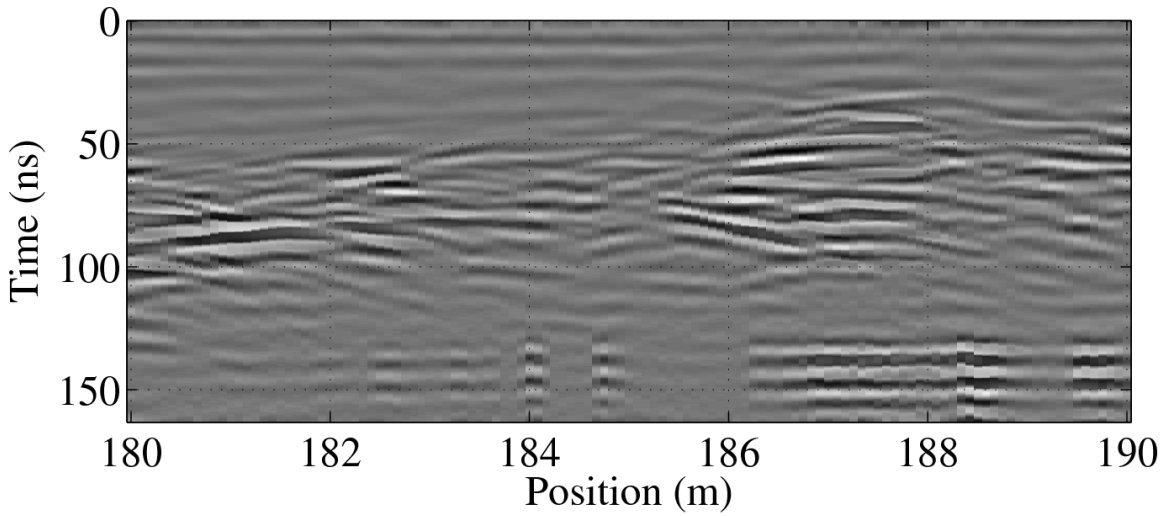

Figure B 15: Profile MUSA001

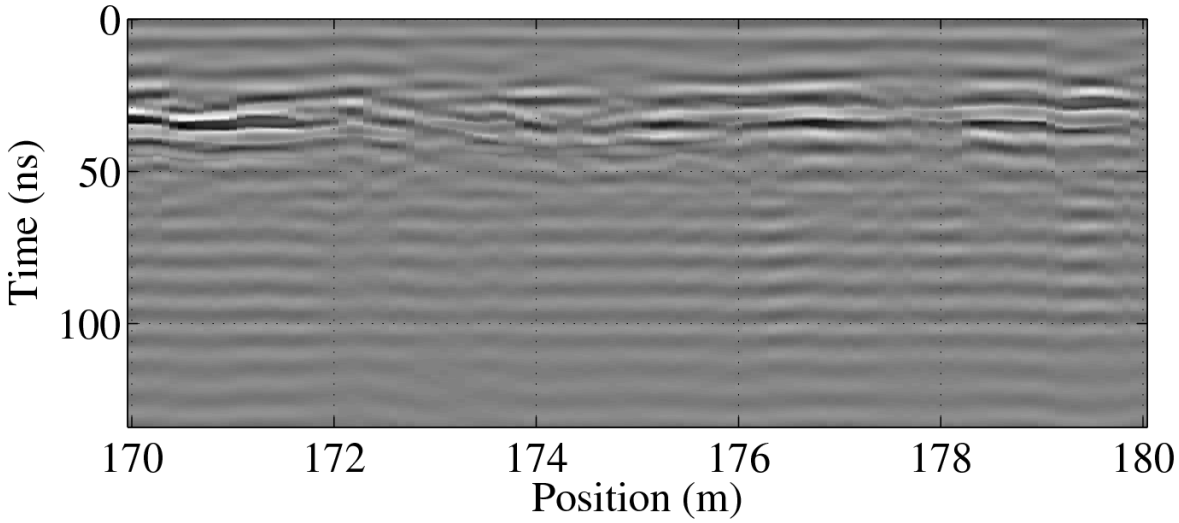

Figure B 16: Profile GJPN2

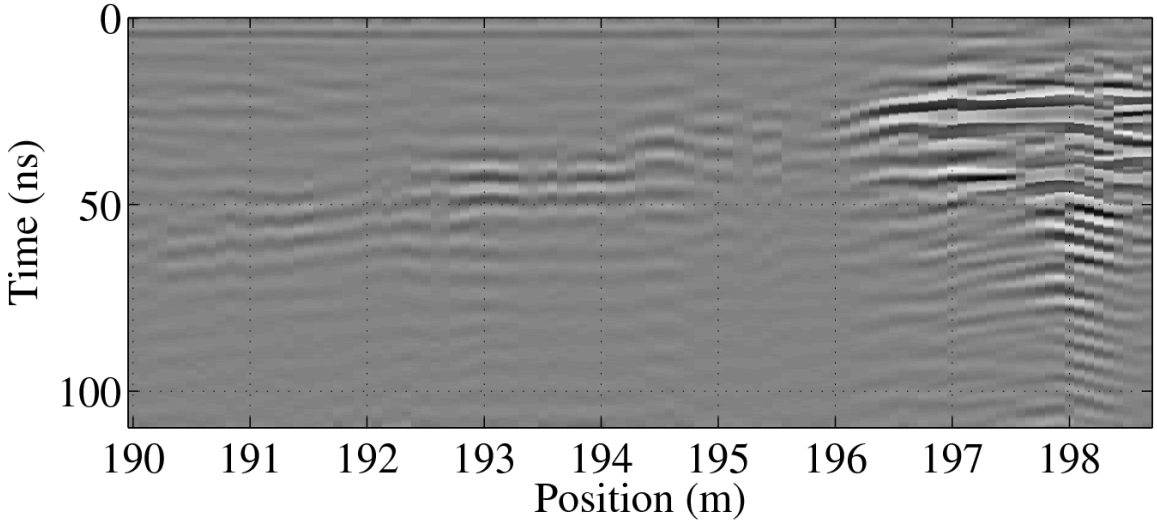

Figure B 17: Profile GJB002

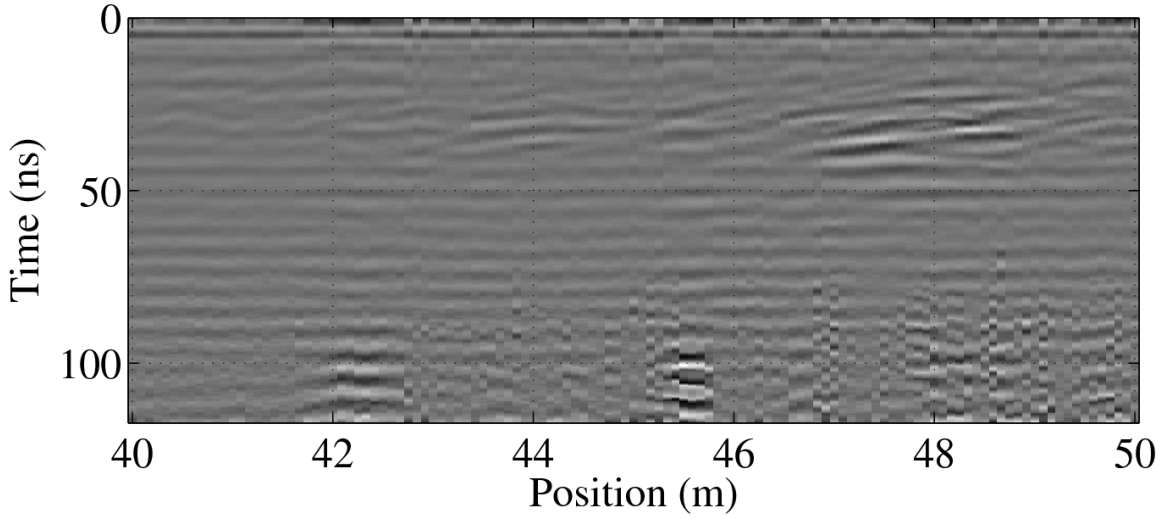

Figure B 18: Profile GJB001

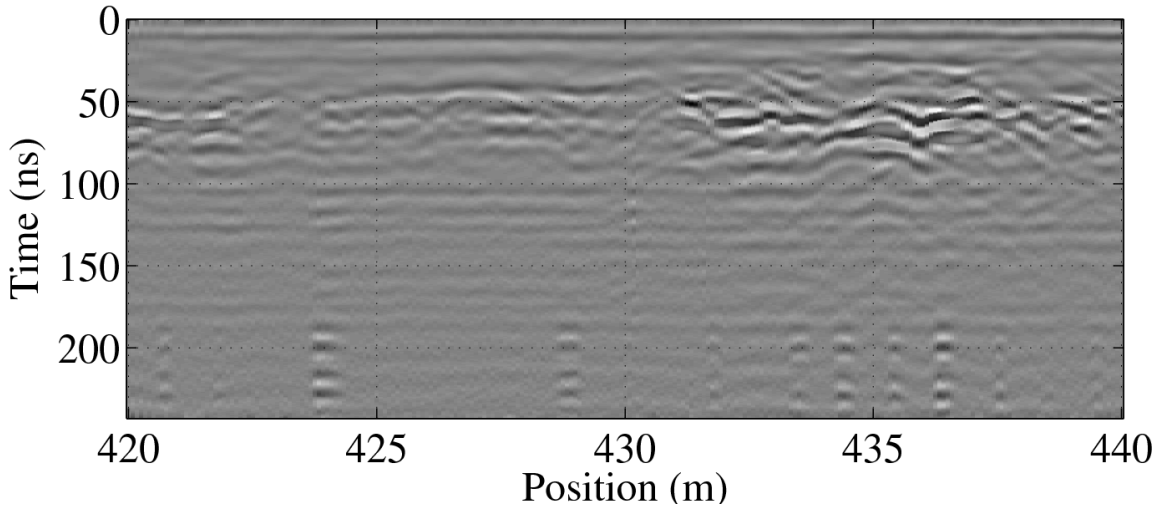

Figure B 19: Profile MUSA004_1

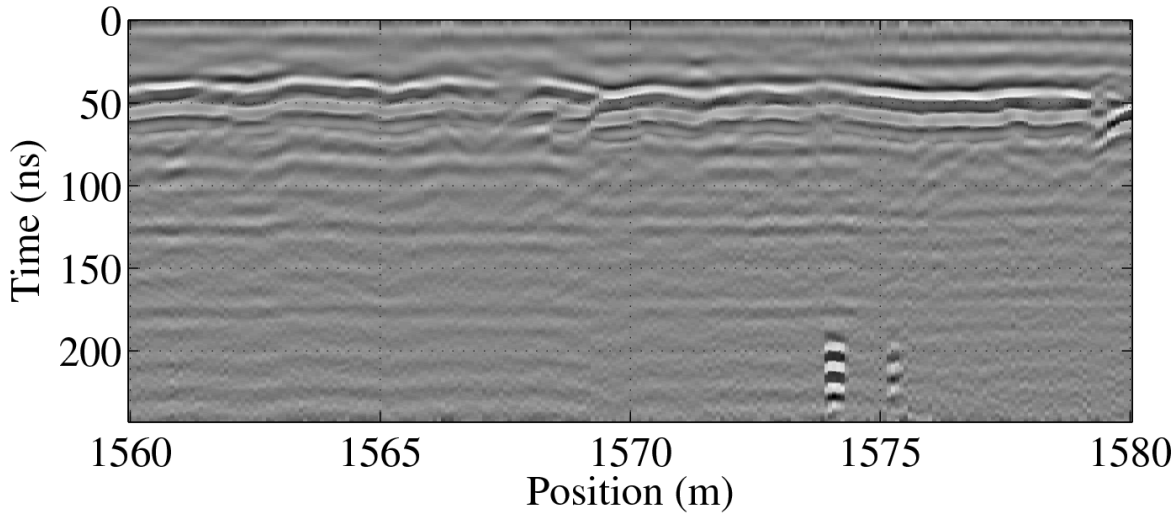

Figure B 20: Profile MUSA004-2

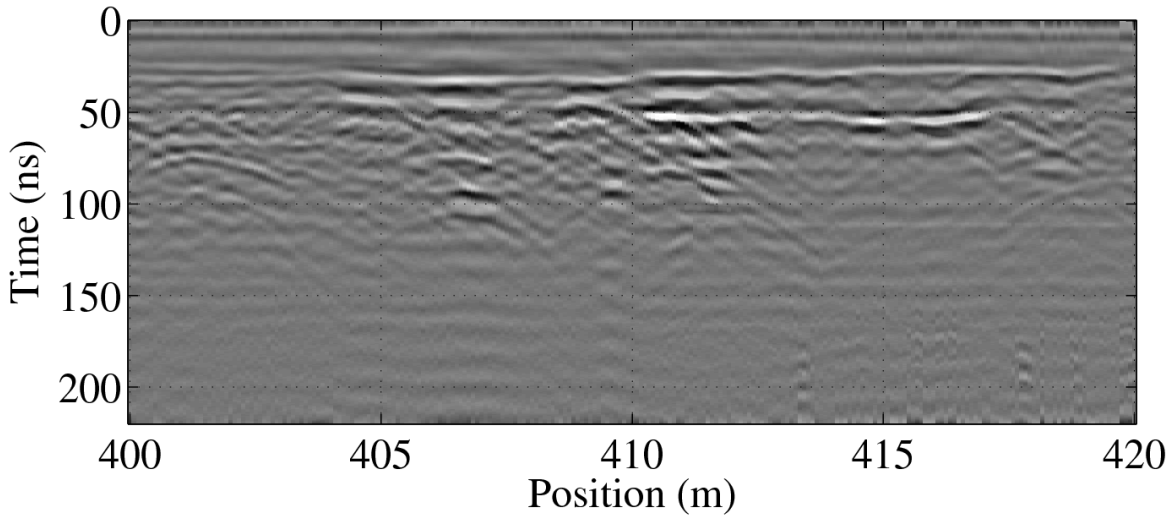

Figure B 21 Profile MUSA 003_1

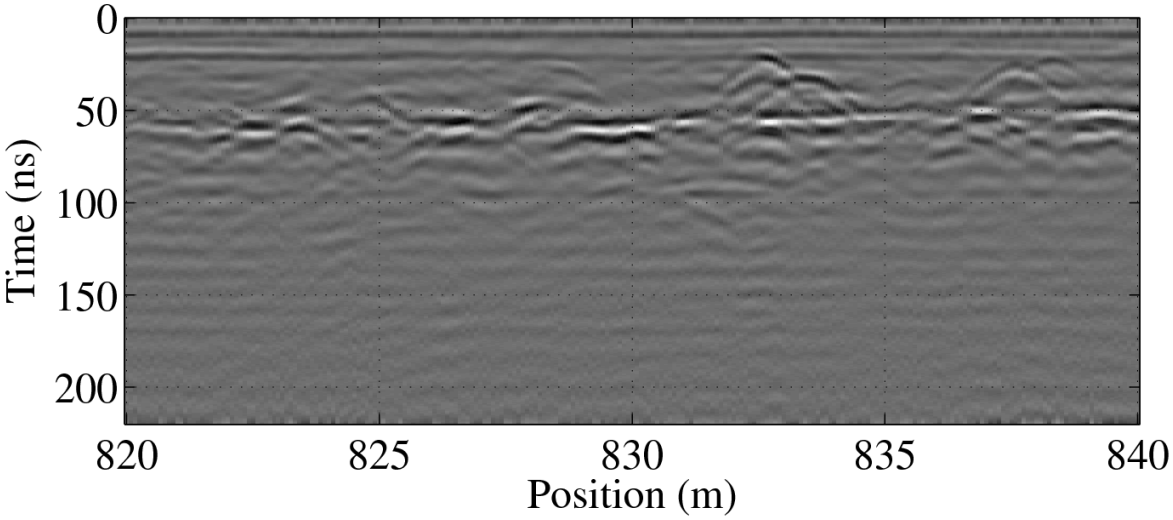

Figure B 22: Profile MUSA 003

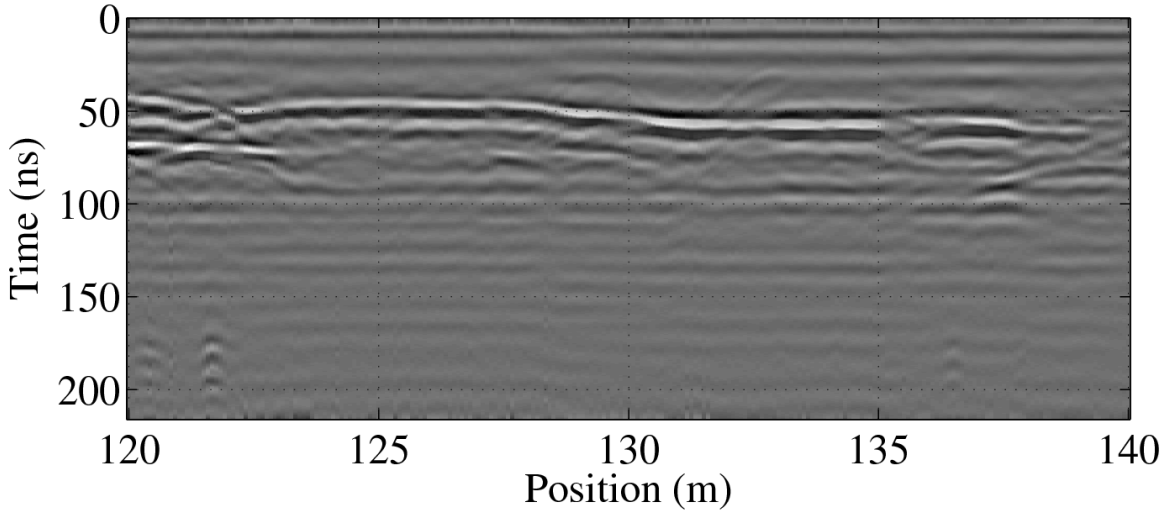

Figure B 23: Profile Musa002

Annex C: Electrical resistivity

Table 9 :ERT survey information

ID	Location	X	Y	Direction	spacing	NorthCable	FailurePins
MU1	Muelledes, 200m W to Pmu1	739368	4547577	N50W	3	4	3;8;12;57
MU2	Muelledes, top hill	739665	4547010	N14W	3	1	3;8;12;57;67
MU3	Muelledes, Pmu1	739484	4547714	N20W	3	1	3;8;12;57;67;70
PN1	Penalbo South, deep well	738440	4553567	N22W	3	1	3;8;12;67;70
GB1	Gejuelo del Barro field W	741062	4551940	N15W	3	4	1-3;8;12;67;70
GB2	Gejuelo del Barro field Pgb0	741348	4551628	N50W	3	1	3;8;12;67;70
GJPN1	Between Gejo and Penalbo, close to Pgjtm0	736646	4555712	N15W	3	4	3;8;12;67;70
GJPN2	Between Gejo and Penalbo, close to Pgjtm0/pond	737020	4555736	N40W	3	4	3;8;12;63;67;70
GJ1	Gejo, close to Pgj0	736066	4557883	N30E	3	1	3;8;12;59;67;70
TB1	Trabadillo	739304	4555923	N105E	5	1	3;8;12;57;67;70
PN2	Penalbo south to deep well	738424	4553345	N50W	5	1	3;8;12;57;67;70
FU1	Prados de la fuente	737051	4549859	N70W	5	1	3;8;12;57;67;70
TM1	Tremedal Est	737302	4551722	N43W	5	4	1;2;3;8;12;57;67;70

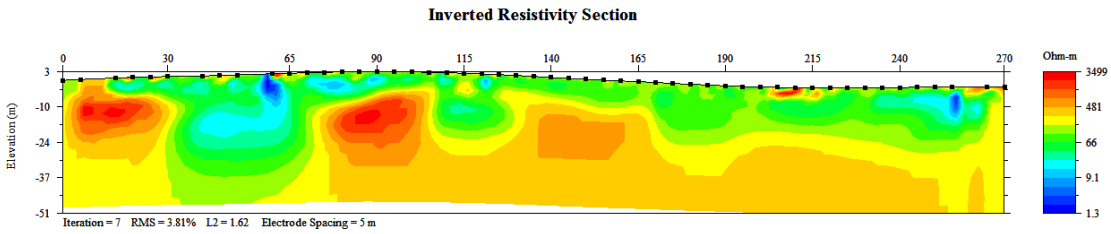

Figure C 1: Inverted resistivity section of FU_1

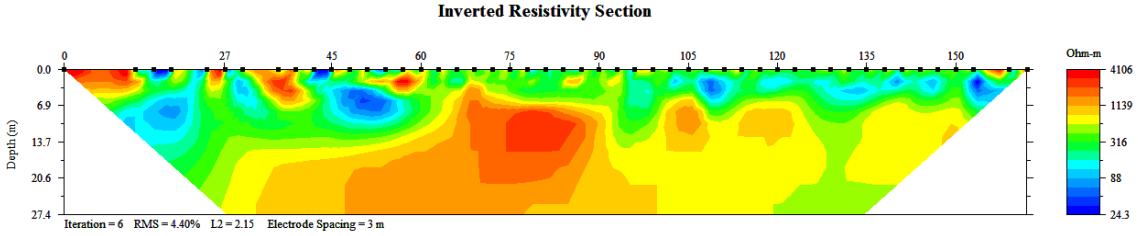

Figure C 2: Inverted resistivity section of GB1

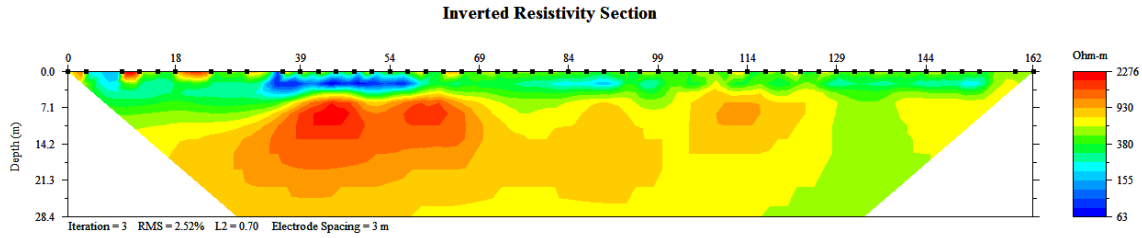

Figure C 3: Inverted resistivity section of GJ1

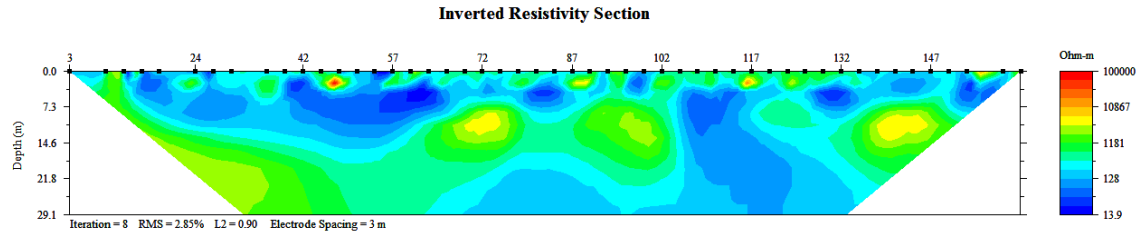

Figure C 4: Inverted resistivity section of GJPN1

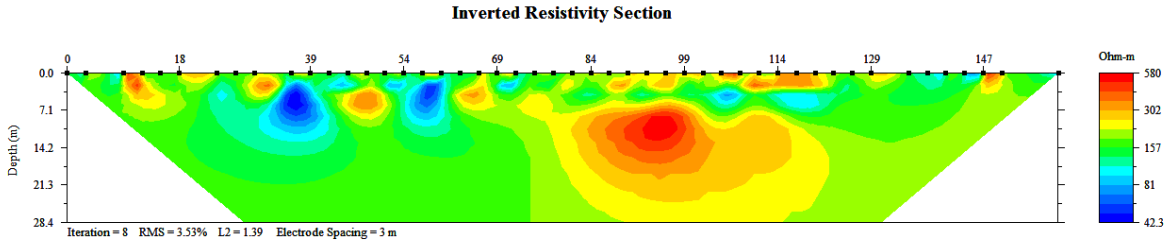

Figure C 5: Inverted resistivity section of GJPN2

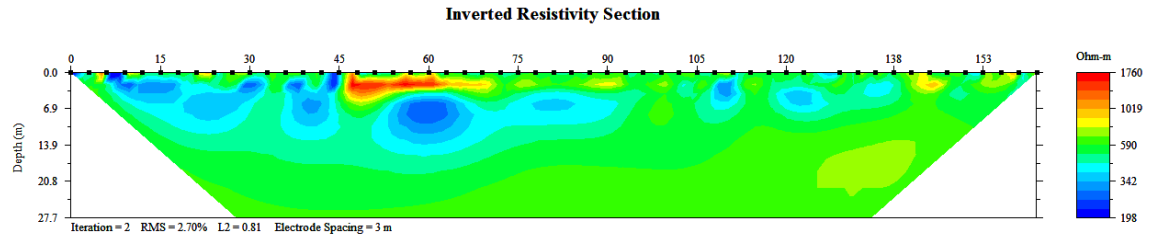

Figure C 6: Inverted resistivity section of MU1

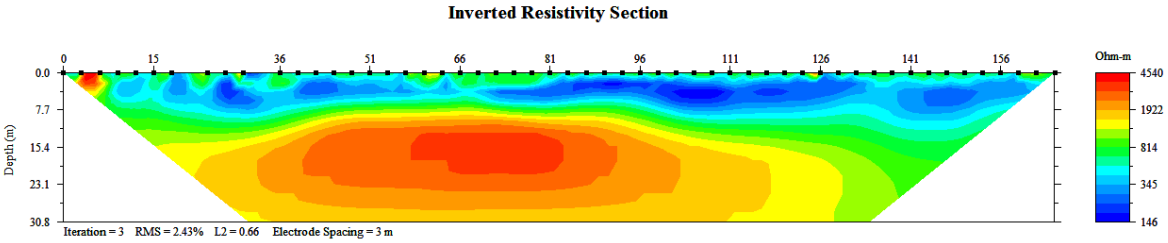

Figure C 7: Inverted resistivity section of MU2

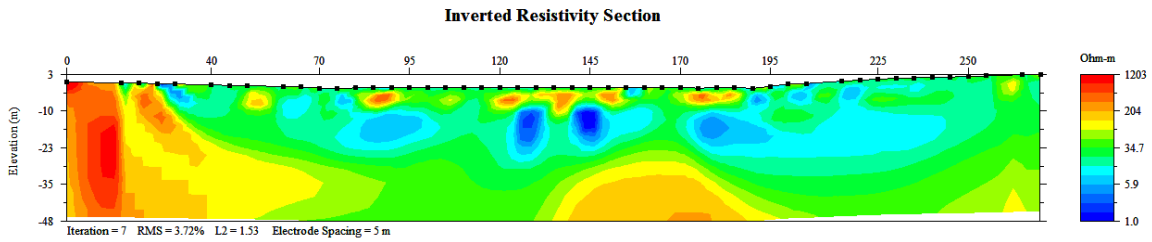

Figure C 8: Inverted resistivity section of TM1

Table 10: VES and ERT points used for interpolation

ID	Location	X	Y	Z	R 1	T 1 (m)	R2	T2 (m)	R3
ID 1	Delta1(Trab)	739551	4555966	741.8	391.8	1.2	70	12.04	202.1
ID 2	Delta2A (Trab	739316	4556056	735.2	824	3.8	22	71.48	3406
ID 3	Gejo1	736119	4557815	808.5	358	0.9	271	4.01	871
ID 4	Gejo2	736330	4557133	789.1	960	4.1	500	9.54	3010
ID 5	Tragejo1	737539	4556468	758.3	331	0.5	20	7.28	40.04
ID 7	Tragejo3	737361	4557528	777.1	388	0.1		87.00	110
ID 8	Gejopen	736475	4555703	778.5	919	1.9	268	30.83	1113
ID 9	Trab1	739138	4555913	740.8	1948	3.0	18	55.00	155
ID 10	Trab2	738875	4556000	754.4	2456	1.0	304	31.00	264
ID 11	Trab4	739500	4555900	738.8	415	1.0	105	24.00	176
ID 12	Tra-vill (VES	740450	4555850	764.9	801	0.9	212	19.00	1286
ID 14	Penalbo2(VES1	736425	4553625	785.0	902	2.2	510	9.29	541
ID 15	Penalbo3(VES1	736575	4553625	780.2	903	2.2	512	9.82	539
ID 17	Penalbo5(VES1	738200	4553625	755.0	154	1.9	12	60.30	808
ID 18	Penalbo6(VES1	739025	4553500	759.4	859	2.2	306	7.51	792
ID 19	Penalbo7(VES1	739650	4553450	769.3	532	1.2	231	22.20	449
ID 20	Penalbo8(VES1	740675	4552950	804.0	1332	1.3	755	8.50	609
ID 22	Penalbo(VES20	738525	4553550	742.0	1142	2.2	19	46.53	6369
ID 24	Alamos (VES1)	738075	4548525	795.2	2849	1.1	350	27.20	2467
ID 26	Varubio(VES5)	740625	4547975	822.1	577	4.0	297	56.00	5999
ID 27	Elgejo	735600	4557263	809.6	692	2.0	124	10.00	854
ID 28	Qpt16	739600	4557150	734.3	941	1.0	182	7.00	109
ID 29	Dykeg11	739350	4546500	836.4	6294	0.3	74	8.44	315
ID 30	Tremed1	737975	4551850	759.0	1993	1.7	14	41.00	1073
ID 31	Tremed2	739200	4551800	777.9	1879	1.0	280	14.00	414
ID 32	VES97A	738375	4548612	782.6	531	3.0	429	94.00	581
ID 33	VES97B	740625	4554325	773.2	995	1.0	398	22.00	517
ID 34	VES97C	740275	4551975	801.3	960	1.0		6.00	1375
ID 35	Gejuelo	739225	4551825	777.9	8792	1.0	669	64.00	1956
ID 37	Wzone	739475	4557050	742.9	168	1.0	21	5.00	88
ID 38	VEST01	740513	4546667	842.7	37.7	6.6	14	8.65	369
ID 39	VEST02	734676	4547701	829.6	823	1.3	176	2.52	559
ID 40	VEST03	736003	4552030	783.3	1198	1.5	239	68.90	14949
ID 41	VEST04	735591	4549124	798.5	2211	2.3	394	79.40	1451
ID 42	VEST05	737117	4549836	767.8	882	1.4	82	19.60	210
ID 43	VEST06	736602	4549835	782.7	690	0.9	238	1.46	1341
ID 44	VEST07	740575	4551275	800.8	2046	0.5	369	14.10	740
ID 45	VEST08	734033	4553428	815.0	10486	0.3	249	17.00	744
ID 46	VEST09	738545	4555690	754.3	1145	0.8	232	95.81	2115
ID 47	VEST10	738604	4555733	753.7	1146	0.8	232	95.47	1540
ID 49	VEST12	739248	4552055	776.6	704	2.1	171	25.40	460
ID 50	VEST13	739433	4552138	778.3	721	2.9	123	2.33	949
ID 51	VEST14	740297	4558326	736.1	607	0.9	334	4.29	249

ID 52	VEST15	735959	4547611	834.3	673	1.3	137	63.50	11988
ID 53	VEST16	736391	4547839	822.3	983	1.0	524	34.60	2319
ID 54	VEST17	736698	4556120	772.9	1424	1.0	351	15.62	692.6
ID 55	VEST18	735243	4557876	809.1	820	1.4	69	1.22	538
ID 56	VEST19	738339	4551938	746.8	725	3.3	27	58.50	4008
ID 57	VEST21	738414	4552860	744.3	1142	4.0	24	43.50	1209
ID 58	fu1 115	737072	4549851	770.4	174.65	5.9	52	17.01	298.9
ID 59	fu1 190	737002	4549877	776.0	120.8	2.1	93	17.51	279
ID 60	GB1 30	741076	4551889	805.3	506.94	0.7	189	10.22	649.3
ID 61	GB1 120	741052	4551976	805.8	301.059	0.7	174	4.00	743.9
ID 62	GB2 150	741297	4551671	804.9	225.45	0.7	105	12.40	331.9
ID 63	GJ 150	736007	4557917	810.8	451.34	0.7	263	7.74	713.7
ID 64	GJPN1 30	736659	4555662	774.6	353.2	2.4	127	10.80	2073
ID 65	GJPN1 60	736652	4555691	775.0	1294.8	0.8	117	10.80	458.6
ID 66	GJPN2 60	737034	4555719	767.8	442.4	2.5	56	11.30	198.3
ID 67	GJPN2 90	737015	4555742	767.5	327.94	2.5	160	8.81	920.6
ID 68	GJPN 2 120	736996	4555765	768.0	316.5	2.5	167	8.81	920.7
ID 69	MU 1 55	739389	4547559	801.4	2951	2.1	402	9.58	2614
ID 70	MU 1 75	739374	4547572	801.2	871.1	2.1	435	11.92	1056
ID 71	MU 2 30	739677	4546959	821.0	779.95	2.2	289	7.74	1460.
ID 72	MU 2 90	739663	4547017	819.9	551.2	0.7	305	5.73	2003
ID 73	MU 2 120	739656	4547046	818.6	669.9	0.7	283	7.75	1257
ID 74	MU 2 150	739648	4547075	818.0	584.7	2.2	284	7.75	759.8
ID 75	MU 3 45	739496	4547679	798.3	699.2	2.1	293	14.24	591
ID 76	MU3 75	739486	4547707	797.6	1197	2.1	306	11.70	558
ID 77	MU3 115	739472	4547745	797.1	2008	2.1	232	7.30	546
ID 78	PN 1 60	738449	4553546	744.0	415.15	3.8	31	20.61	208.8
ID 79	PN 1 90	738437	4553574	743.6	121.21	2.2	45	20.61	1486
ID 80	PN 2 60	738483	4553295	745.8	234.17	1.3	81	8.23	533.7
ID 81	PN2 180	738391	4553372	743.7	377.2	2.6	24	32.84	191.7
ID 82	PN2 250	738337	4553417	744.5	1637.8	0.9	70	11.09	222.2
ID 83	TB1 60	739379	4555903	737.1	210.7	1.2	30	20.66	122.5
ID 84	TB1120	739321	4555918	735.6	259.65	3.7	19	35.46	185
ID 85	TB1 150	739292	4555926	736.0	105.93	1.2	26	16.60	510
ID 86	TM1 40	737368	4551651	755.3	1318.5	1.7	80	14.02	239.4
ID 87	TM1 140	737300	4551724	754.6	297.75	6.0	43	27.89	162.1